



THE UNIVERSITY *of* EDINBURGH

Edinburgh Research Explorer

## The decadal state of the terrestrial carbon cycle: global retrievals of terrestrial carbon allocation, pools and residence times

### Citation for published version:

Bloom, A, Exbrayat, J-F, Van der Velde, I, Feng, L & Williams, M 2016, 'The decadal state of the terrestrial carbon cycle: global retrievals of terrestrial carbon allocation, pools and residence times' Proceedings of the National Academy of Sciences, vol. 113, no. 5. DOI: 10.1073/pnas.1515160113

### Digital Object Identifier (DOI):

[10.1073/pnas.1515160113](https://doi.org/10.1073/pnas.1515160113)

### Link:

[Link to publication record in Edinburgh Research Explorer](#)

### Document Version:

Peer reviewed version

### Published In:

Proceedings of the National Academy of Sciences

### Publisher Rights Statement:

<http://www.sherpa.ac.uk/romeo/issn/1091-6490/>

### General rights

Copyright for the publications made accessible via the Edinburgh Research Explorer is retained by the author(s) and / or other copyright owners and it is a condition of accessing these publications that users recognise and abide by the legal requirements associated with these rights.

### Take down policy

The University of Edinburgh has made every reasonable effort to ensure that Edinburgh Research Explorer content complies with UK legislation. If you believe that the public display of this file breaches copyright please contact [openaccess@ed.ac.uk](mailto:openaccess@ed.ac.uk) providing details, and we will remove access to the work immediately and investigate your claim.



1 **The decadal state of the terrestrial carbon cycle: global retrievals**  
2 **of terrestrial carbon allocation, pools and residence times**

3

4 **A. Anthony Bloom<sup>1,2,3</sup>, Jean-François Exbrayat<sup>2,3</sup>, Ivar van der Velde<sup>4</sup>, Liang Feng<sup>2,3</sup>,**  
5 **Mathew Williams<sup>2,3</sup>**

6

7 **1. Jet Propulsion Laboratory, California Institute of Technology, Pasadena, CA, USA**

8 **2. School of GeoSciences, University of Edinburgh, Edinburgh, UK**

9 **3. National Centre for Earth Observation, Edinburgh, UK**

10 **4. Wageningen University, Wageningen, The Netherlands**

11

12 **Corresponding author: A. Anthony Bloom (abloom@jpl.nasa.gov)**

13

14 **Biological Sciences: Environmental Sciences**

15

16 **Abstract**

17

18 The terrestrial carbon cycle is currently the least constrained component of the global  
19 carbon budget. Large uncertainties stem from a poor understanding of plant carbon  
20 allocation, stocks, residence times and carbon use efficiency. Imposing observational  
21 constraints on the terrestrial carbon cycle and its processes is therefore necessary to  
22 better understand its current state and to predict its future state. We combine a

23 diagnostic ecosystem carbon model with satellite observations of leaf area and biomass  
24 (where and when available) and soil carbon data to retrieve the first global estimates of  
25 carbon cycle state and process variables at a  $1^{\circ}\times 1^{\circ}$  resolution; retrieved variables are  
26 independent from the plant functional type and steady-state paradigms. Our results  
27 reveal global emergent relationships in the spatial distribution of key carbon cycle states  
28 and processes. Live biomass and dead organic carbon residence times exhibit  
29 contrasting spatial features ( $r=0.3$ ). Allocation to structural carbon is highest in the wet  
30 tropics (85–88%) in contrast to higher latitudes (73–82%), where allocation shifts  
31 towards photosynthetic carbon. Carbon use efficiency is lowest (0.42–0.44) in the wet  
32 tropics. We find an emergent global correlation between retrievals of leaf mass per leaf  
33 area and leaf lifespan ( $r=0.64$ – $0.80$ ) that matches independent trait studies. We show  
34 that conventional land-cover types cannot adequately describe the spatial variability of  
35 key carbon states and processes (multiple correlation median: 0.41). This mismatch has  
36 strong implications for the prediction of terrestrial carbon dynamics, which is currently  
37 based on globally applied parameters linked to land-cover or plant functional types.

38

### 39 **Significance**

40

41 Quantitative knowledge of terrestrial carbon pathways and processes is fundamental for  
42 understanding the biosphere's response to a changing climate. Carbon allocation, stocks  
43 and residence times together define the dynamic state of the terrestrial carbon cycle.  
44 These quantities are difficult to measure and remain poorly quantified on a global scale.

45 Here we retrieve global  $1^{\circ}\times 1^{\circ}$  carbon state and process variables by combining a carbon  
46 balance model with satellite observations of biomass and leaf area (where and when  
47 available) and global soil carbon data. Our results reveal emergent continental-scale  
48 patterns and relationships between carbon states and processes. We find conventional  
49 land-cover types cannot capture continental-scale variations of retrieved carbon  
50 variables: this mismatch has strong implications for terrestrial carbon cycle predictions.

51

52 **© 2015. All rights reserved.**

53

54 **Keywords:** carbon cycle, LAI, biomass, soil carbon, model-data fusion, allocation,  
55 residence time.

56 \body

57 **Introduction**

58

59 The terrestrial carbon (C) cycle remains the least constrained component of the global C  
60 budget (1). In contrast to a relatively stable increase of the ocean CO<sub>2</sub> sink from 0.9 Pg C  
61 yr<sup>-1</sup> to 2.7 Pg C yr<sup>-1</sup> over the past 40 years, terrestrial CO<sub>2</sub> uptake has been found to vary  
62 between a net 4.1 Pg C yr<sup>-1</sup> sink to a 0.4 Pg C yr<sup>-1</sup> source, and accounts for a majority of  
63 the inter-annual variability in atmospheric CO<sub>2</sub> growth. The complex response of  
64 terrestrial ecosystem CO<sub>2</sub> exchanges to short- and long-term changes in temperature,  
65 water availability, nutrient availability and rising atmospheric CO<sub>2</sub> (2– 6) remain highly  
66 uncertain in C cycle model projections (7). As a result, there are large gaps in our

67 understanding of terrestrial C dynamics, including the magnitude and residence times of  
68 the major ecosystem C pools (8, 9) and rates of autotrophic respiration (10). Moreover,  
69 the impact of climatic extremes on C cycling, such as recent Amazon droughts (11),  
70 highlights the importance of understanding the terrestrial C cycle sensitivity to climate  
71 variability. To understand terrestrial CO<sub>2</sub> exchanges in the past, present and future, we  
72 need to better constrain current dynamics of ecosystem C cycling, from regional to  
73 global scales.

74

75 C uptake, allocation, pool stocks, residence times, respiration and disturbance together  
76 drive net CO<sub>2</sub> exchanges (12) on sub-daily to millennial timescales; these C state and  
77 process variables also determine the temporal sensitivity of the net C balance to climatic  
78 variability. For example, global changes in photosynthetic uptake could lead to a rapid  
79 response from short-lived C pools (such as foliage, fine roots and litter), or to a  
80 prolonged response from the long-lived C pools (such as woody biomass and soil C),  
81 with very different outcomes on ecosystem source/sink behavior. Quantitative  
82 knowledge of terrestrial C pathways is therefore central to understanding the temporal  
83 responses of the major terrestrial C fluxes – including heterotrophic respiration (13),  
84 fires (14, 15) and wetland CH<sub>4</sub> emissions (16, 17) – to inter-annual variations in C uptake.

85

86 While C dynamics have been extensively measured and analyzed at site-level (18– 21),  
87 the respiration and allocation of fixed C, and its residence time within the major C pools,  
88 are difficult and expensive to measure at site level, and remain poorly quantified on

89 global scales. As a result, global terrestrial C cycle models rely on land-cover type  
90 specific C cycling parameters – based on spatially pre-assigned plant functional types –  
91 to determine C fluxes and C pools (22). Globally spanning C cycle observations can  
92 provide a much-needed constraint on the spatial variability and associated dynamics of  
93 the terrestrial C cycle. Over the past decade a growing number of datasets have  
94 enhanced understanding of the terrestrial C cycle, including global scale canopy  
95 dynamics (NASA Moderate Resolution Imaging Spectroradiometer – MODIS leaf area  
96 index – LAI – and burned area products), empirically derived global soil C data  
97 (Harmonized World Soil Database – HWSD, 23), satellite-based above and below ground  
98 biomass maps for the tropics (ABGB, 24, 25), and Greenhouse Gases Observing Satellite  
99 (GOSAT) CO<sub>2</sub> and plant fluorescence (26, 27). These spatially and temporally explicit  
100 datasets provide an enhanced view of the terrestrial C cycle, and can be used together  
101 to retrieve consistent global C state and process variables. Significant efforts in data-  
102 driven estimates of the global C fluxes have been made over the past decade. These  
103 include estimates based on atmospheric CO<sub>2</sub> concentrations (1, 28, 29); high-resolution  
104 global primary production maps (30) based on FLUXNET eddy covariance tower datasets  
105 (18); the mean residence time of terrestrial C (31); ecosystem respiration dependence  
106 on temperature, based on FLUXNET data (32) and global C cycle data assimilation  
107 systems (33).

108

109 Given an increasing number of C cycle observations, what remains an outstanding  
110 challenge is to produce a data-consistent analysis of terrestrial C cycling – including

111 retrievals of C fluxes, C pools, autotrophic respiration, allocation fractions and residence  
112 times – based on multiple global-scale earth observations and datasets. Current global-  
113 scale terrestrial biosphere models, due to their complexity and structures, are ill-  
114 equipped to ingest an ever-increasing volume of earth observations to estimate (instead  
115 of prescribing) model parameters, based on the currently available observations. To  
116 overcome this challenge, we use a model-data fusion (MDF) approach to retrieve  
117 terrestrial C state and process variables during the period 2001–10, without invoking  
118 plant functional type or steady-state assumptions. We bring together global MODIS LAI,  
119 a tropical biomass map (24), a soil C dataset (23), MODIS burned area (34), and a  
120 diagnostic ecosystem C balance model (DALEC2, 19, 35) to retrieve C state and process  
121 variables by producing a novel data-consistent and spatially explicit analysis of  
122 terrestrial C cycling on a global  $1^{\circ}\times 1^{\circ}$  grid (Fig. 1; we henceforth refer to this model-data  
123 fusion setup as the CARbon DATA MOdel framework, or CARDAMOM). Specifically, we  
124 address the following questions: how is C uptake partitioned between the live biomass  
125 pools and respiration? What is the residence time of C within the major ecosystem C  
126 pools? How do estimates of C cycle states and processes vary spatially and to what  
127 degree do emergent variable patterns match land-cover maps? We use a Markov Chain  
128 Monte Carlo MDF algorithm to retrieve C state and process variables – and their  
129 associated uncertainty – within each  $1^{\circ}\times 1^{\circ}$  degree grid cell (see Materials and Methods).  
130 The MDF approach retrieves the state and process variables that minimize the model  
131 mismatch against any available C cycle observations. Therefore, in the absence of extra-

132 tropical biomass data or winter-time MODIS LAI observations, estimates of 2001–10 C  
133 cycle state and process variables are achievable, albeit more uncertain.

134

## 135 **Results**

136

137 Distinct C allocation patterns emerge from our terrestrial C analysis (Fig. 2). Net primary  
138 production (NPP) allocation to structural biomass (wood and fine roots) is largely  $\geq 80\%$   
139 (area-weighted 25<sup>th</sup> – 75<sup>th</sup> %ile range = 85–88%) in the wet tropics ( $< 23^\circ\text{N/S}$ ; annual  
140 precipitation  $> 1500\text{mm}$ ), in contrast to the dry tropics (77–87%), and extra-tropical  
141 regions (73–82%). The highest NPP allocations to foliage ( $\geq 30\%$ ) spatially coincide with  
142 major grassland areas, including the North America prairies, Central Asia steppes and  
143 the Sahel region in Africa. The dry tropics exhibit relatively high NPP allocation to labile  
144 C (7–14%; Fig. S1); this reflects the increasing impact of seasonality on production as  
145 precipitation declines, requiring labile C stores for leaf flush. Carbon use efficiency (CUE  
146 =  $1 - \text{autotrophic respiration fraction}$ ) is overall lowest in within the wet tropics (0.42–  
147 0.44) in contrast to the dry tropics (0.45–0.50), temperate ( $23\text{--}55^\circ\text{N/S}$ ; 0.47–0.50) and  
148 high latitudes ( $> 55^\circ\text{N/S}$ ; 0.49–0.50).

149

150 Live biomass and dead organic C residence times exhibit contrasting spatial features ( $r =$   
151 0.3; Fig. 3). Within the majority of wet tropical land area (56%) – especially across most  
152 of the Amazon (76%) and Congo (69%) river basins– the longest C residence time occurs  
153 within the woody pool (Fig. S1). In the dry tropics and extra-tropical latitudes, soil C



154 residence times exceed wood C residence time by a median factor of 2.6 (1.6–4.3).  
155 Woody residence time is typically shorter in the dry tropics (8–19 yrs) compared to  
156 other biomes (wet tropics: 12–21 yrs; temperate: 21–29 yrs; high latitudes: 25–28 yrs).  
157 Litter C residence time is typically longer in extra-tropical ecosystems (0.8–1.6 yrs) in  
158 comparison to tropical ecosystems (0.4–0.5 yrs). The longest foliar residence time (or  
159 leaf lifespan) occurs in the wet tropics and semi-arid regions (Fig. S1).

160

161 Overall, the wet tropics are characterized by relatively high structural C ( $>100 \text{ tC ha}^{-1}$ )  
162 and photosynthetic C ( $>2.5 \text{ tC ha}^{-1}$ ) (Fig. 4): in contrast, the dry tropics and extra-tropical  
163 regions exhibit less structural and/or photosynthetic C. Foliar C stocks are typically  
164 larger in the wet tropics ( $2.8\text{--}4.7 \text{ tC ha}^{-1}$ ) relative to other biomes ( $0.2\text{--}0.6 \text{ tC ha}^{-1}$ );  
165 similarly, fine root stocks are also greater in the wet tropics ( $4.0\text{--}5.3 \text{ tC ha}^{-1}$ ), compared  
166 to other biomes ( $0.8\text{--}2.7 \text{ tC ha}^{-1}$ ). Root:shoot (fine root C:leaf C) is lowest in the wet  
167 tropics (1.1–1.5), followed by the dry tropics (1.6–1.9) and extra-tropics (1.8–2.1). We  
168 find larger woody C uncertainties ( $1^\circ \times 1^\circ$  90% confidence range / median) in the extra-  
169 tropics (1.8–4.6) in contrast to tropical woody C (1.4–1.6) due to the latitudinal limits of  
170 the total above- and below-ground biomass map (24). Litter C is greater in high latitudes  
171 ( $2.4\text{--}3.4 \text{ tC ha}^{-1}$ ) relative to temperate ( $0.6\text{--}2.4 \text{ tC ha}^{-1}$ ) and tropical ( $0.2\text{--}2.6 \text{ tC ha}^{-1}$ )  
172 regions. High-latitude ecosystems have higher labile C stocks linked to seasonal leaf  
173 expansion ( $0.2\text{--}0.5 \text{ tC ha}^{-1}$ ) relative to temperate ( $0.1\text{--}0.3 \text{ tC ha}^{-1}$ ) and tropical ( $0.1\text{--}0.3$   
174  $\text{tC ha}^{-1}$ ) ecosystems.

175

176 We find high leaf C mass per leaf area (LCMA) values in the wet tropics (85-97 gC m<sup>-2</sup>),  
177 and in semi-arid regions, such as the Sahel, South-western United States and the  
178 Australian continent (typically >100 gC m<sup>-2</sup>; Fig. 5); LCMA estimates are lower (typically  
179 <80 gC m<sup>-2</sup>) in high latitudes and the dry tropics. We find a positive correlation between  
180 leaf lifespan and LCMA in high-latitude ( $r = 0.79$ ), temperate ( $r = 0.80$ ), dry tropical ( $r =$   
181  $0.78$ ) and wet tropical ( $r = 0.64$ ) areas.

182

183 Global GPP (global 25<sup>th</sup> – 75<sup>th</sup> %ile = 91–134 Pg C yr<sup>-1</sup>), ecosystem respiration (91–137 Pg  
184 C yr<sup>-1</sup>) and fires (1.3–2.0 Pg C yr<sup>-1</sup>) are broadly consistent with the MSTMIP terrestrial  
185 carbon model ensemble (22), data-driven estimates (36) and bottom-up inventories (37)  
186 (Fig. S5). The Net Carbon Exchange uncertainty (-8 to +13 Pg C yr<sup>-1</sup>) is an order of  
187 magnitude greater than mode NCE (-2 Pg C yr<sup>-1</sup>); NCE latitudinal uncertainty is larger but  
188 comparable to the MSTMIP model range. Global atmospheric model CO<sub>2</sub> concentrations  
189 based on CARDAMOM mode NCE fluxes are seasonally consistent ( $r^2 = 0.93$ ,  $RMSE =$   
190  $0.53$  ppm CO<sub>2</sub>) with mean total column CO<sub>2</sub> measurements (38, Fig. S6). The mean  
191 integrated C residence time by (31) is within the range of individual pool residence times  
192 at locations B, T, D and W (Fig. 3). The 2001–10 CARDAMOM analysis spatial and  
193 temporal LAI variability is consistent with the MODIS LAI constraints ( $r^2 = 0.8$ ;  $RMSE =$   
194  $0.6$  m<sup>2</sup>/m<sup>2</sup>). When alternative GPP (36), alternative model structure or biased data  
195 constraints ( $\pm 20\%$ ) are imposed at locations B, T, D and W, 88% of median sensitivity  
196 analysis estimates are within  $\pm 50\%$  of median C state and process variable retrievals  
197 (Fig. S2).

198

199 Retrieved C cycle variables are broadly consistent with a range of in-situ measurements  
200 (Table S3). Estimates of CUE within the Amazon river basin are comparable to the upper  
201 bound of recent measurements (0.32–0.47)(39). Recent estimates of extra-tropical  
202 forest C density (40) are on average 38% lower than CARDAMOM total biomass  
203 estimates within forested areas (although these are typically within the CARDAMOM  
204  $1^{\circ}\times 1^{\circ}$  uncertainty). Estimates of mean Amazon woody C residence times (15–21 yrs) are  
205 lower but comparable to above-ground woody C residence times derived from site-level  
206 measurements (~20–70 yrs; 20).

207

208 We find that 88-99% of C state and process variability is accounted for by 8 empirical  
209 orthogonal basis functions (EOFs, Fig. 6); in other words, retrieved C state and process  
210 variables are largely explained by eight modes of spatial variability (Fig. S4). On average,  
211 GLOBCOVER land-cover type classifications (41, e.g. deciduous forests, evergreen forests  
212 and grasslands) account for <50% of C state and process variability (median multiple  
213 correlation coefficient  $R = 0.41$ ); GLOBCOVER land-cover types best describe spatial  
214 variations in C stocks ( $0.5\leq R\leq 0.8$ ), followed by LCMA ( $R = 0.4$ ), residence times  
215 ( $0.3\leq R\leq 0.5$ ) and allocation fractions ( $0.1\leq R\leq 0.4$ ).

216

217 **Discussion**

218

219 Typically C allocation and residence time parameters are based on land-cover types in  
220 global-scale terrestrial C cycle studies (9, 22, amongst others); here, spatially broad  
221 allocation and residence patterns emerge instead, as a result of the model-data fusion  
222 approach. For example, high biomass ecosystems throughout the wet tropics display  
223 similar C allocation, residence time and LCMA configurations (Fig. 2–5). Similarly, we  
224 find that dead organic matter (DOM) C residence is generally longer in high latitudes  
225 (Fig. 3). In comparison to conventional land-cover types, EOFs 1-4 account for a larger  
226 degree of the spatial structures in retrieved C variables (Fig. 6); for most variables, the  
227 two dominant EOF modes – which together reflect first-order variations in latitude and  
228 global precipitation patterns (Fig. S4) – explain more spatial variability than GLOBCOVER  
229 land-cover types. The mismatch between land-cover types and retrieved variables has  
230 major implications for the estimation and prediction of terrestrial C cycling, which is  
231 currently based on small sets of globally applied parameters linked to land-cover types.  
232 The importance of climate, biodiversity, fire and anthropogenic disturbance in  
233 generating these mismatches needs to be explored in further research (42).

234

235 It also is clear that plant traits vary across biomes (Fig. 2-4, S1), not just at biome  
236 boundaries (43), and that there are continental-scale trade-offs and correlations among  
237 traits (44). Our analysis is consistent with these viewpoints: for example, the emergent  
238 relationship between LCMA (proportional to leaf mass per area) and leaf lifespan (Fig. 5)  
239 matches the positive correlation found in global plant trait datasets (45). Evaluating  
240 global plant-trait patterns emerging from CARDAMOM provides a novel opportunity for

241 connections to theoretical and functional biodiversity research, and a route to  
242 integrating this knowledge into predictive terrestrial C cycle modeling.  
243  
244 The residence times of major C stocks provide substantial insights into the sensitivity  
245 and potential future trajectories of the terrestrial C cycle. For example, land-cover  
246 changes in the wet tropics may result in rapid DOM C losses, given the relatively short  
247 DOM residence times (<30 yrs) (Fig. 3). In contrast, high-latitude C residence times are  
248 an order of magnitude higher (30–300 yrs), and therefore shifts in C allocation or  
249 turnover rates are likely to result in long-lived C flux responses. Overall, given the  
250 predominant role of C residence times in future terrestrial uptake responses (9), the  
251 derived residence times provide a first-order estimate of ecosystem response times as a  
252 result of changes in C cycling regimes. However, we note that model structure is likely to  
253 be a major source of uncertainty in long-lived (>10yr) C flux predictions. For example,  
254 while reduced complexity models can capture some of the principal long-term (>10yr)  
255 DOM dynamics represented in earth system models (46) systematic errors in DOM  
256 dynamics can arise due to the under-representation of processes controlling DOM  
257 residence times (47, 48). We also note that our decadal analysis is unlikely to be able to  
258 capture slow feedback processes acting on longer time-scales such as permafrost re-  
259 mobilization and priming (49). The large allocation and stocks and short residence time  
260 of wood in the wet tropics indicates the potentially rapid potential for regrowth and C  
261 accumulation post-disturbance (50). We note that fires are less frequent but major

262 events within boreal ecosystems (51), and therefore longer time-periods are required  
263 for retrievals to fully account for the effect of fires on high-latitude C residence times.  
264  
265 C state and process variable retrievals are sensitive to the uncertainty characteristics of  
266 C cycle observations (35) and the prior parameter ranges (Table S1). We highlight that  
267 the current coverage and accuracy of C cycle observations (24, 52) remains a major  
268 limiting factor in our approach. For example, temperate and high-latitude C stock and  
269 residence time uncertainties are higher due to the absence of biomass observations.  
270 Undoubtedly, future estimates of globally-spanning biomass density will provide a major  
271 constraint on CARDAMOM estimates of extra-tropical C state and process variables (53).  
272  
273 Land-to-atmosphere C flux estimates could be used to further constrain CARDAMOM C  
274 fluxes (Fig. S5) and C cycle variables associated to non-steady C states. For example, soil  
275 C residence time samples are negatively correlated with corresponding mean 2001–10  
276 NCE samples at locations B ( $r = -0.3$ ), T ( $r = -0.4$ ), D ( $r = -0.5$ ) and W ( $r = -0.3$ ); therefore,  
277 regional- or grid-scale estimates of NCE could provide a much-needed additional  
278 constraint on soil C residence time. CARDAMOM flux magnitude and uncertainty can be  
279 used as prior information in global atmospheric CO<sub>2</sub> inversions; in turn, the assimilation  
280 of GOSAT and OCO-2 atmospheric CO<sub>2</sub> observations (54) should further constrain  
281 CARDAMOM NCE estimates and their associated uncertainties. In this manner, non-  
282 steady state C fluxes can ultimately be reconciled with ecosystem state and process  
283 variables, such as C stocks and residence times.

284

285 The CARDAMOM approach provides a framework to test alternative model structures  
286 (55): in this manner, combined C cycle model parametric and structural uncertainties  
287 can be characterized, while ensuring consistency between models and global-scale  
288 datasets. This assessment would amount to a major step forward from conventional C  
289 cycle model inter-comparison studies. Ultimately an ensemble of models can be used to  
290 determine the degree to which retrievals of key C state and process variables are model-  
291 dependent. Moreover, alternative model structures could be used in CARDAMOM to  
292 assimilate globally spanning plant traits related to C cycling (56) and satellite  
293 observations such as solar-induced fluorescence (27), vegetation optical depth (57), soil  
294 moisture (58, 59) and changes in above-ground biomass (25, 60, 61). We anticipate that  
295 the incorporation of additional datasets and alternative model structures into  
296 CARDAMOM will generate quantifiable reductions in retrieved C variable uncertainties  
297 and new ecological insights on the state of terrestrial C cycle.

298

## 299 **Materials and Methods**

300

301 We grid MODIS LAI, ABGB (24), and HWSD topsoil and subsoil (0-100cm) C density (23)  
302 at a 1°×1° resolution (section S1 of the SI). The Data Assimilation Linked Ecosystem  
303 Carbon model version two (DALEC2) is analytically described by (35); an overview of  
304 DALEC2 C fluxes and pools is shown in Fig. 1. The 17 DALEC2 parameters (controlling the  
305 processes of photosynthesis and phenology, allocation, and turnover rates) and six

306 initial C pools robustly characterize terrestrial ecosystem C balance (19). DALEC2 is a  
307 generic representation of C-cycling, where plant-functional types (PFTs) are not explicit:  
308 instead, model parameters are treated as unknown and independent quantities for each  
309 1°×1° grid cell (Table S1). We incorporate a fire C loss parameterization to account for  
310 seasonal and inter-annual variations in fire C fluxes from DALEC2 (section S2 of the SI).  
311 The model drivers consist of monthly time-step ERA interim meteorology and MODIS  
312 burned area (34) at a 1°×1° resolution.

313

314 For each 1° x 1° grid cell, we use Bayesian inference to retrieve the probability of  
315 DALEC2 model parameters  $\mathbf{x}_i$  (Table S1) given observational constraints  $\mathbf{O}_i$ , henceforth  
316  $\mathbf{p}(\mathbf{x}_i | \mathbf{O}_i)$ , where

317

$$318 \mathbf{p}(\mathbf{x}_i | \mathbf{O}_i) \propto \mathbf{p}(\mathbf{x}_i) \mathbf{p}(\mathbf{O}_i | \mathbf{x}_i) \quad (1)$$

319

320  $\mathbf{p}(\mathbf{x}_i)$  is the prior parameter information and  $\mathbf{p}(\mathbf{O}_i | \mathbf{x}_i)$  is the likelihood of  $\mathbf{x}_i$  with respect to  
321  $\mathbf{O}_i$ . We use a Markov Chain Monte Carlo algorithm to sample  $\mathbf{x}_i$  from  $\mathbf{p}(\mathbf{x}_i | \mathbf{O}_i)$ : we  
322 henceforth refer to the retrieved DALEC2 parameter values at pixel  $i$  as  $\mathbf{y}_i$ . Within each  
323 grid cell, C allocation fractions, residence times within each C pool, stocks, LCMA, and  
324 associated C fluxes are derived from 4000 samples of  $\mathbf{y}_i$  (section S3 of the SI). We hence  
325 obtain a probability density function (PDF) for all C cycle variables within each 1°×1° grid  
326 cell.

327



328 We do not impose PFT specific prior parameter distributions, or steady state  
329 assumptions:  $\mathbf{p}(\mathbf{x}_i)$  consists of ecologically viable parameter ranges (Table S1) and  
330 ecological and dynamical constraints (35). Together these guarantee ecologically  
331 consistent parameter retrievals within a globally prescribed parameter space, without  
332 imposing spatially explicit prior parameter information.

333

334 From the C state and process variable estimates within each  $1^\circ \times 1^\circ$  grid cell we use 4000  
335 samples of  $\mathbf{y}_i$  to determine the mean, median, mode, and %ile ranges for each C state  
336 and process variable ranges. In Fig. 2-4, we present C allocation, residence time and C  
337 stock 5<sup>th</sup>, 25<sup>th</sup>, median, 75<sup>th</sup> and 95<sup>th</sup> %iles at four selected locations: **B**: boreal [62.5°N,  
338 81.5°E]; **T**: temperate [40.5°N, 120.5°W]; **D**: dry tropics [12.5°N, 20.5°E] and **W**: wet  
339 tropics [7.5°S, 60.5°W]. We chose **B**, **T**, **D** and **W** as representative examples for C state  
340 and process variable values within each area (the full  $1^\circ \times 1^\circ$  C state and process variable  
341 maps are shown in Fig. S1). To determine the robustness of our C state and process  
342 variable estimates, we perform dedicated sensitivity tests to characterize the role of  
343 systematic errors in data constraints and model structure: we repeat our C variable  
344 retrievals using  $\pm 20\%$  LAI,  $\pm 20\%$  ABGB,  $\pm 20\%$  HWSD,  $\pm 20\%$  combustion coefficients,  
345 alternative GPP (36) and limited heterotrophic respiration at  $< 0^\circ\text{C}$  (section S4 of the SI).

346

347 We compare our results against in-situ and regional observations of C allocation, pools  
348 and residence times (section S5 of the SI), and we evaluate the resulting fluxes against  
349 atmospheric  $\text{CO}_2$  observations across 12 Total Carbon Column Observing Network sites

350 (38) by incorporating NCE results in a 4D atmospheric transport model (29). To  
351 determine whether global land-cover types can predict the spatial variability of our  
352 results, we conduct a multiple correlation coefficient analysis between C state and  
353 process variables and 18 GLOBCOVER land-cover fractions at  $1^\circ \times 1^\circ$ . We also employed a  
354 principal component analysis on C state and process variables to retrieve the primary  
355  $1^\circ \times 1^\circ$  empirical orthogonal functions (EOFs). The details of the CARDAMOM results  
356 evaluation and analyses are fully described in sections S5-8 of the SI. Statistical  
357 abbreviations throughout the text include  $r$  (Pearson correlation coefficient),  $RMSE$   
358 (root-mean-square error). All spatially derived  $r$  and  $RMSE$  values reported in the text  
359 are area-weighted. Retrieved C variable ranges – reported as area-weighted 25<sup>th</sup> – 75<sup>th</sup>  
360 %iles – are derived from  $1^\circ \times 1^\circ$  mean allocation and C stocks, log-based mean C  
361 residence times (Fig. S1) and median LCMA values (Fig. 6). All CARDAMOM datasets  
362 presented in this study can be downloaded from [datashare.is.ed.ac.uk/](http://datashare.is.ed.ac.uk/handle/10283/875)  
363 [handle/10283/875](http://datashare.is.ed.ac.uk/handle/10283/875).

364

### 365 **Acknowledgements**

366

367 AAB, JE, LF and MW were funded by the NERC National Centre for Earth Observation  
368 (NCEO), UK. This work made use of the Edinburgh Compute and Data Facility resources  
369 (ECDF, [ecdf.ed.ac.uk](http://ecdf.ed.ac.uk)). The research leading to these results has received funding from  
370 the European Union's FP7 (2007-2013) under grant agreement no. 283080, project  
371 GEOCARBON. IV was financially supported under a Netherlands Organization for

372 Scientific Research project (VIDI: 864.08.012). The TCCON Network is supported by  
373 NASA's Carbon Cycle Science Program through a grant to the California Institute of  
374 Technology. Part of this research was carried out at the Jet Propulsion Laboratory,  
375 California Institute of Technology, under a contract with the National Aeronautics and  
376 Space Administration.

377

### 378 **Contributions**

379 AAB and MW conceived the research. AAB undertook the research with assistance from  
380 JE, IV, MW and LF. AAB and MW wrote the paper with assistance from the other  
381 authors.

382

### 383 **References**

384

385 1. Le Quéré C, et al. (2013) The global carbon budget 1959–2011. *Earth System Sci Data* 5(1): 165-185.

386

387 2. Gatti LV, et al. (2014) Drought sensitivity of Amazonian carbon balance revealed by atmospheric measurements.

388 *Nature* 506(7486): 76-80.

389

390 3. Dieleman WIJ, et al. (2012) Simple additive effects are rare: a quantitative review of plant biomass and soil process  
391 responses to combined manipulations of CO<sub>2</sub> and temperature. *Global Change Biol* 18(9): 2681-2693.

392

393 4. Keenan TF, et al. (2013) Increase in forest water-use efficiency as atmospheric carbon dioxide concentrations rise.

394 *Nature* 499(7458): 324-327.

395

- 396 5. Reich PB, Hobbie SE (2013) Decade-long soil nitrogen constraint on the CO<sub>2</sub> fertilization of plant biomass. *Nature*  
397 *Clim Change* 3(3): 278-282.
- 398
- 399 6. Schimel D, Stephens BB, Fisher JB (2015) Effect of increasing CO<sub>2</sub> on the terrestrial carbon cycle. *Proc Natl Acad Sci*  
400 112(2): 436-441.
- 401
- 402 7. Cox PM, et al. (2013) Sensitivity of tropical carbon to climate change constrained by carbon dioxide variability.  
403 *Nature* 494(7437): 341-344.
- 404
- 405 8. Todd-Brown KEO, et al. (2013) Causes of variation in soil carbon simulations from CMIP5 Earth system models and  
406 comparison with observations. *Biogeosci* 10(3): 1717-1736.
- 407
- 408 9. Friend AD, et al. (2014) Carbon residence time dominates uncertainty in terrestrial vegetation responses to future  
409 climate and atmospheric CO<sub>2</sub>. *Proc Natl Acad Sci* 111(9): 3280-3285.
- 410
- 411 10. Atkin OK, et al. (2015) Global variability in leaf respiration in relation to climate, plant functional types and leaf  
412 traits. *New Phytol* 206(2): 614-636.
- 413
- 414 11. Lewis SL, Brando PM, Phillips OL, van der Heijden GMF, Nepstad D (2011) The 2010 Amazon Drought. *Science*  
415 331(6017): 554-554.
- 416
- 417 12. Luo, Y, Weng E (2011) Dynamic disequilibrium of the terrestrial carbon cycle under global change. *Trends in Ecol &*  
418 *Evol* 26(2): 96-104.
- 419
- 420 13. Trumbore S (2006) Carbon respired by terrestrial ecosystems—recent progress and challenges. *Glob Change Biol*  
421 12(2): 141-153.
- 422
- 423 14. Randerson JT, et al. (2005) Fire emissions from C3 and C4 vegetation and their influence on interannual variability  
424 of atmospheric CO<sub>2</sub> and δ<sup>13</sup>CO<sub>2</sub>. *Glob Biogeochem Cycles* 19(2)

- 425
- 426 15. Bloom AA, et al. (2015) Remote-sensing constraints on South America fire traits by Bayesian fusion of atmospheric  
427 and surface data. *Geophys Res Lett* 42(4): 1268-1274.
- 428
- 429 16. Bloom AA, Palmer PI, Fraser A, Reay DS (2012) Seasonal variability of tropical wetland CH<sub>4</sub> emissions: the role of  
430 the methanogen-available carbon pool. *Biogeosci* 9(8): 2821-2830.
- 431
- 432 17. Melton JR, et al. (2013) Present state of global wetland extent and wetland methane modelling: conclusions from  
433 a model intercomparison project (WETCHIMP). *Biogeosci* 10: 753-788.
- 434
- 435 18. Baldocchi D, et al. (2001) FLUXNET: A new tool to study the temporal and spatial variability of ecosystem-scale  
436 carbon dioxide, water vapor, and energy flux densities. *Bull Am Meteorol Soc* 82(11): 2415-2434.
- 437
- 438 19. Williams M, Schwarz PA, Law BE, Irvine J, Kurpius MR (2005) An improved analysis of forest carbon dynamics using  
439 data assimilation *Glob Change Biol* 11(1): 89-105.
- 440
- 441 20. Malhi Y, Saatchi S, Girardin C, Aragão LEOC (2009) The production, storage, and flow of carbon in Amazonian  
442 forests. *Amazonia and Glob Change* (2009): 355-372.
- 443
- 444 21. De Kauwe MG, et al. (2014) Where does the carbon go? A model–data intercomparison of vegetation carbon  
445 allocation and turnover processes at two temperate forest free-air CO<sub>2</sub> enrichment sites. *New Phytol* 203(3): 883-899.
- 446
- 447 22. Huntzinger DN, et al. (2013) The north american carbon program multi-scale synthesis and terrestrial model  
448 intercomparison project–part 1: Overview and experimental design. *Geosci Model Development* 6(6): 2121-2133.
- 449
- 450 23. Hiederer R, Köchy M (2011) Global Soil Organic Carbon Estimates and the Harmonized World Soil Database. *EUR*  
451 *25225 EN*. Publications Office of the European Union. 79pp.
- 452

- 453 24. Saatchi SS, et al. (2011) Benchmark map of forest carbon stocks in tropical regions across three continents. *Proc*  
454 *Natl Acad Sci* 108(24): 9899-9904.
- 455
- 456 25. Baccini AGSJ, et al. (2012) Estimated carbon dioxide emissions from tropical deforestation improved by carbon-  
457 density maps. *Nature Clim Change* 2(3):182-185.
- 458
- 459 26. Yokota T, et al. (2009) Global concentrations of CO<sub>2</sub> and CH<sub>4</sub> retrieved from GOSAT: First preliminary results. *Sola*  
460 5: 160-163.
- 461
- 462 27. Frankenberg C, et al. (2011) New global observations of the terrestrial carbon cycle from GOSAT: Patterns of plant  
463 fluorescence with gross primary productivity. *Geophys Res Lett* 38(17).
- 464
- 465 28. Peters W, et al. (2010) Seven years of recent European net terrestrial carbon dioxide exchange constrained by  
466 atmospheric observations. *Glob Change Biol* 16(4): 1317-1337.
- 467
- 468 29. Feng L, et al. (2011) Evaluating a 3-D transport model of atmospheric CO<sub>2</sub> using ground-based, aircraft, and space-  
469 borne data. *Atmospheric Chem and Phys* 11(6): 2789-2803.
- 470
- 471 30. Beer C, et al. (2010) Terrestrial gross carbon dioxide uptake: global distribution and covariation with climate.  
472 *Science* 329(5993): 834-838.
- 473
- 474 31. Carvalhais N, et al. (2014) Global covariation of carbon turnover times with climate in terrestrial ecosystems.  
475 *Nature* 514: 213–217.
- 476
- 477 32. Mahecha MD, et al. (2010) Global convergence in the temperature sensitivity of respiration at ecosystem level.  
478 *Science* 329(5993): 838-840.
- 479
- 480 33. Ziehn T, Scholze M, Knorr W (2012) On the capability of Monte Carlo and adjoint inversion techniques to derive  
481 posterior parameter uncertainties in terrestrial ecosystem models. *Glob Biogeochem Cycles* 26(3).

482

483 34. Giglio L, Randerson JT, van der Werf GR (2013) Analysis of daily, monthly, and annual burned area using the  
484 fourth-generation global fire emissions database (GFED4). *J Geophys Res: Biogeosci* 118(1): 317-328.

485

486 35. Bloom AA, Williams M. (2015) Constraining ecosystem carbon dynamics in a data-limited world: integrating  
487 ecological "common sense" in a model–data fusion framework. *Biogeosci* 12(5): 1299-1315.

488

489 36. Jung M, Reichstein M, Bondeau A (2009) Towards global empirical upscaling of FLUXNET eddy covariance  
490 observations: validation of a model tree ensemble approach using a biosphere model. *Biogeosci* (6)10: 2001-2013.

491

492 37. van der Werf GR, et al. (2010) Global fire emissions and the contribution of deforestation, savanna, forest,  
493 agricultural, and peat fires (1997–2009). *Atmospheric Chem and Phys* 10(23): 11707-11735.

494

495 38. Wunch D, et al. (2011) The total carbon column observing network. *Phil Trans Roy Soc A*, 369(1943): 2087-2112.

496

497 39. Malhi Y, et al. (2015) The linkages between photosynthesis, productivity, growth and biomass in lowland  
498 Amazonian forests. *Glob Change Biol* 21(6): 2283-2295.

499

500 40. Thurner M. et al. (2014) Carbon stock and density of northern boreal and temperate forests. *Global Ecology and*  
501 *Biogeography* 23(3): 297-310.

502

503 41. Bontemps, S., et al. (2011) GLOBCOVER 2009-Products description and validation report.

504

505 42. Lehmann CER, et al. (2014) Savanna vegetation-fire-climate relationships differ among continents. *Science*  
506 343(6170): 548-552.

507

508 43. Reich PB, et al. (2014) Biogeographic variation in evergreen conifer needle longevity and impacts on boreal forest  
509 carbon cycle projections. *Proc Natl Acad Sci* 111(38): 13703-13708.

510

511 44. Sterck F, et al. (2011) Functional traits determine trade-offs and niches in a tropical forest community. *Proc Natl*  
512 *Acad Sci* 108(51): 20627-20632.  
513

514 45. Wright IJ, et al. (2004) The worldwide leaf economics spectrum. *Nature* 428(6985): 821-827.  
515

516 46. Todd-Brown KE, et al. (2013) Causes of variation in soil carbon simulations from CMIP5 Earth system models and  
517 comparison with observations. *Biogeosci* 10(3): 1717-1736  
518

519 47 Trumbore, S (2000) Age of soil organic matter and soil respiration: radiocarbon constraints on belowground C  
520 dynamics. *Ecol Appl* 10(2): 399-411.  
521

522 48: Doetterl S, Six J, van Wesemael B, van Oost K (2012) Carbon cycling in eroding landscapes: geomorphic controls on  
523 soil organic C pool composition and C stabilization. *Glob Change Biol* 18(7): 2218-2232.  
524

525 49: Wild B, et al. (2014) Input of easily available organic C and N stimulates microbial decomposition of soil organic  
526 matter in arctic permafrost soil. *Soil Biol Biochem*, 75: 143-151.  
527

528 50. Exbrayat J, Williams M (2015) Quantifying the net contribution of the historical Amazonian deforestation to  
529 climate change. *Geophys Res Lett* 42.8: 2968-2976.  
530

531 51. Amiro BD, Stocks BJ, Alexander ME, Flannigan MD, Wotton BM (2001) Fire, climate change, carbon and fuel  
532 management in the Canadian boreal forest. *Internat J of Wildland Fire* 10(4): 405-413.  
533

534 52. Heiskanen J, et al (2012) Seasonal variation in MODIS LAI for a boreal forest area in Finland. *Remote Sens of*  
535 *Environ*, 126: 104-115.  
536

537 53. Schimel D, et al. (2015) Observing terrestrial ecosystems and the carbon cycle from space. *Glob change biol*, 21(5):  
538 1762-1776.  
539



- 540 54. Crisp D, Miller CE, DeCola PL (2008) NASA Orbiting Carbon Observatory: measuring the column averaged carbon  
541 dioxide mole fraction from space. *J Applied Remote Sens* 2(1): 23508.
- 542
- 543 55. Keenan TF, Carbone MS, Reichstein M, Richardson A (2011) The model–data fusion pitfall: assuming certainty in  
544 an uncertain world. *Oecologia* 167(3): 587-597.
- 545
- 546 56. Kattge J, et al. (2011) TRY—a global database of plant traits. *Glob Change Biol* 17(9): 2905-2935.
- 547
- 548 57. Lawrence H, et al. (2014) Comparison between SMOS Vegetation Optical Depth products and MODIS vegetation  
549 indices over crop zones of the USA. *Remote Sens of Environ* 140: 396-406.
- 550
- 551 58. Kerr YH, et al. (2010) The SMOS mission: New tool for monitoring key elements of the global water cycle. *Proc of*  
552 *the IEEE* 98,(5): 666-687.
- 553
- 554 59. Entekhabi D, et al. (2010) The soil moisture active passive (SMAP) mission. *Proc of the IEEE* 98(5): 704-716.
- 555
- 556 60. Le Toan T, et al. (2011) The BIOMASS mission: Mapping global forest biomass to better understand the terrestrial  
557 carbon cycle. *Remote Sens of Environ* 115(11): 2850-2860.
- 558
- 559 61. Liu YY, et al. (2015) Recent reversal in loss of global terrestrial biomass. *Nature Clim Change* 5:470-474.
- 560
- 561 62. DeLucia EH, Drake JE, Thomas RB, Gonzales-Meler M (2007) Forest carbon use efficiency: is respiration a constant  
562 fraction of gross primary production? *Glob Change Biol* 13(6): 1157-1167.
- 563
- 564 63. Feng L, et al. (2015) Elevated uptake of CO<sub>2</sub> over Europe inferred from GOSAT XCO<sub>2</sub> retrievals: a real phenomenon  
565 or an artefact of the analysis? *Atmos Chem and Phys Discus* 15(2): 1989-2011.
- 566
- 567 64. Huntzinger DN, et al. (2015, in press). NACP MsTMIP: Global 0.5-deg Terrestrial Biosphere Model Outputs (version  
568 1) in Standard Format. Dataset available on-line [<http://daac.ornl.gov>]. DOI: 10.3334/ORNLDAAC/1225

569

570 65. Metcalfe DB, et al. (2008) The effects of water availability on root growth and morphology in an Amazon

571 rainforest. *Plant and Soil* 311(1-2) 189-199.

572

573 66. Burke MK, Raynal DJ (1994) Fine root growth phenology, production, and turnover in a northern hardwood forest

574 ecosystem. *Plant and soil* 162(1): 135-146.

575

576 67. Gill RA, Jackson RB (2000) Global patterns of root turnover for terrestrial ecosystems. *New Phytol* 147(1): 13-31.

577

578 68. Sloan VL, Fletcher BJ, Press MC, Williams M, Phoenix GK (2013) Leaf and fine root carbon stocks and turnover are

579 coupled across Arctic ecosystems. *Glob Change Biol* 19(12): 3668-3676.

580

## 581 **Figure captions**

582

583 **Fig. 1:** Diagnostic ecosystem carbon (C) balance model DALEC2 (19,35) and datasets

584 used to retrieve  $1^\circ \times 1^\circ$  C state and process variables. Gross primary production (GPP), a

585 function of climate and foliar C, is partitioned into autotrophic respiration ( $R_a$ ) and net

586 primary production (NPP). NPP is partitioned into the live biomass pools. Plant mortality

587 provides input to the dead organic matter (DOM) pools. Heterotrophic respiration ( $R_h$ )

588 is derived from decomposing DOM pools. Fire fluxes are derived from burned area data

589 (35) and all C pools (see section S3). Within each  $1^\circ \times 1^\circ$  grid cell, we use a Bayesian

590 model-data fusion algorithm to retrieve C state/process variables and uncertainties;

591 variables are retrieved without prior land-cover type or steady state assumptions. Data

592 constraints consist of MODIS leaf area, total biomass (24, tropics only) and soil C (23).

593 Details on the Bayesian fusion approach are provided in the Materials and Methods  
594 section.

595

596 **Fig. 2:** Retrievals of net primary production (NPP) allocation to structural (wood and fine  
597 roots) and photosynthetic (labile and foliage) C pools. Allocation fractions were  
598 retrieved at  $1^{\circ} \times 1^{\circ}$  using a Bayesian model-data fusion approach (Fig. 1). The gross  
599 primary production allocation fraction retrievals at locations B, T, D and W are shown in  
600 the three right-hand panels (median = black dot, 50% confidence range = box and 90%  
601 confidence range = line).

602

603 **Fig. 3:** Retrievals of C residence time (RT) in live biomass and dead organic matter C  
604 pools; residence times are retrieved at  $1^{\circ} \times 1^{\circ}$  using a Bayesian model-data fusion  
605 approach (Fig. 1). Brown colors denote ecosystems with high residence times for all C  
606 pools, green areas denote ecosystems with long live biomass C residence times and  
607 orange areas denote ecosystems with low live biomass residence time. The residence  
608 times for individual C pools at locations B, T, D and W are shown in the three right-hand  
609 panels (median = black dot, 50% confidence range = box and 90% confidence range =  
610 line). Mean C residence times by (31) are shown as grey boxes (50% confidence interval)  
611 and black dots (median).

612

613 **Fig.4:** Retrieved mean photosynthetic (foliar and labile) and structural (wood and fine  
614 roots) C pool stocks; C stocks are retrieved at  $1^{\circ} \times 1^{\circ}$  using a Bayesian model-data fusion

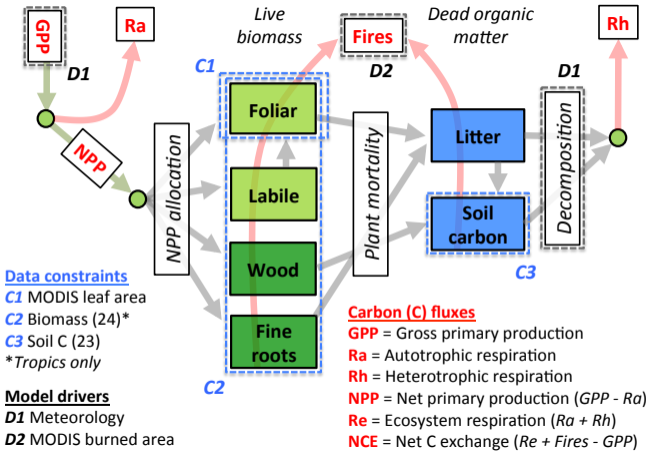
615 approach (Fig. 1). Retrieved mean C stocks for each pool at locations B, T, D and W are  
616 shown in the four right-hand panels (median = black dot, 50% confidence range = box  
617 and 90% confidence range = line). Dark colors denote high structural C/high  
618 photosynthetic C ecosystems, green colors denote low structural C/high photosynthetic  
619 C ecosystems, red colors denote low photosynthetic C/high structural C ecosystems, and  
620 yellow colors denote low photosynthetic C/low structural C ecosystems.

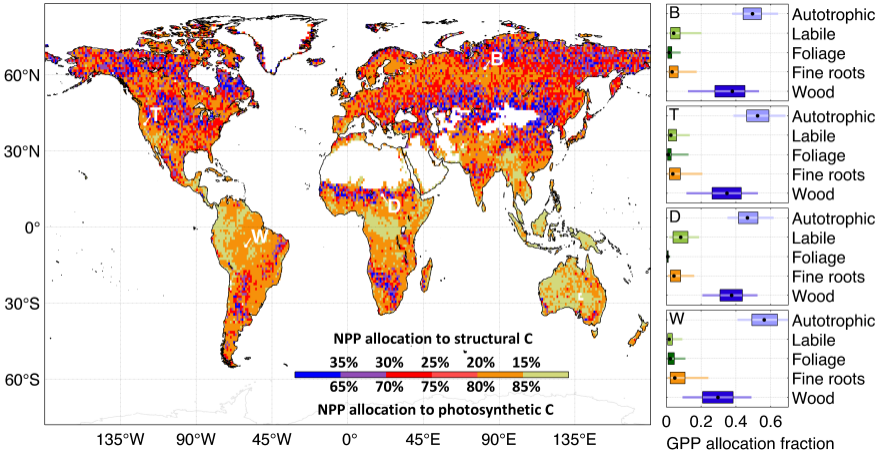
621

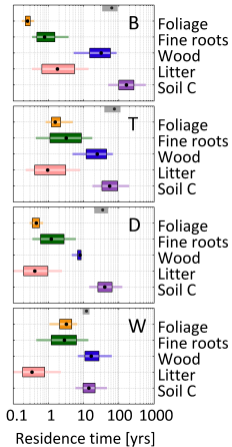
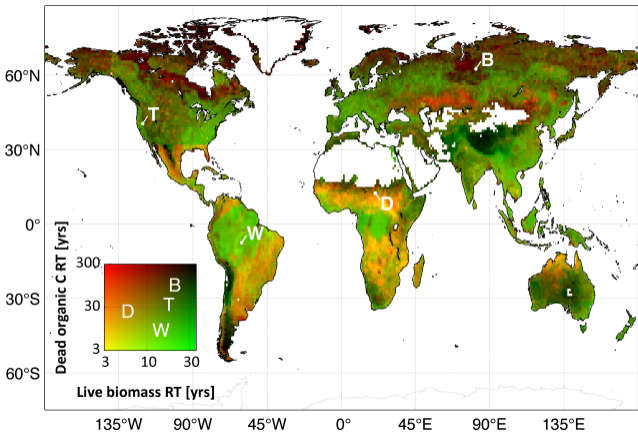
622 **Fig. 5. Top:** Retrieved median  $1^\circ \times 1^\circ$  leaf C mass per leaf area (LCMA,  $\text{gC m}^{-2}$ ). **Top right:**  
623 zonal mean of median LCMA and 50% confidence range. **Bottom:** LCMA against leaf  
624 lifespan for high latitudes ( $>55^\circ\text{N/S}$ ), temperate regions ( $23^\circ\text{--}55^\circ\text{N/S}$ ), dry tropics  
625 (precip. $<1500\text{mm}$ ,  $<23^\circ\text{N/S}$ ) and wet tropics (precip. $>1500\text{mm}$ ,  $<23^\circ\text{N/S}$ ).

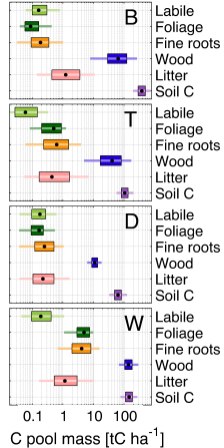
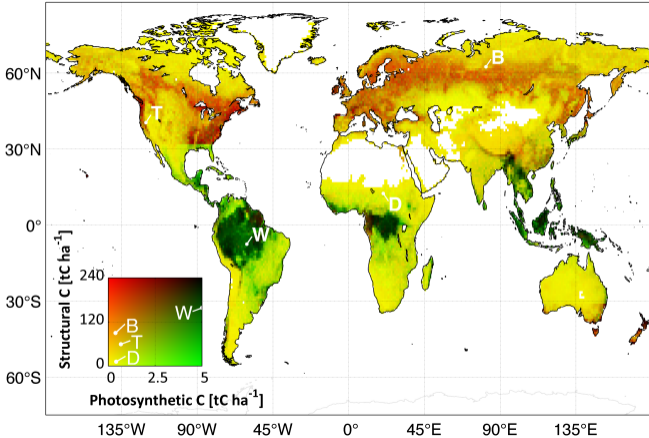
626

627 **Fig. 6.** Multiple correlation coefficients (R, x-axis) of retrieved C state and process  
628 variables (allocation fractions, residence times, mean C pools and LCMA; y-axis) against  
629 18 GLOBCOVER land-cover fractions and C variable primary empirical orthogonal  
630 functions (EOFs). R denotes the ability of GLOBCOVER land-cover types and primary  
631 EOFs to predict  $1^\circ \times 1^\circ$  state and process variables (R would equal 1 if all C state and  
632 process variables could be expressed as a linear sum of land-cover fractions or EOFs).

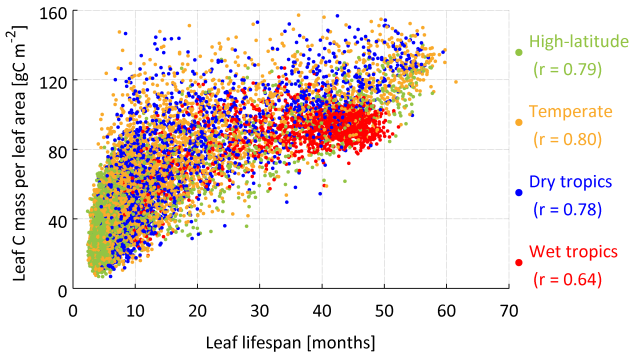
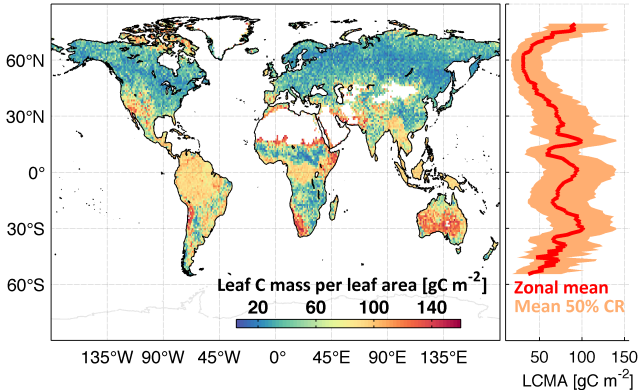


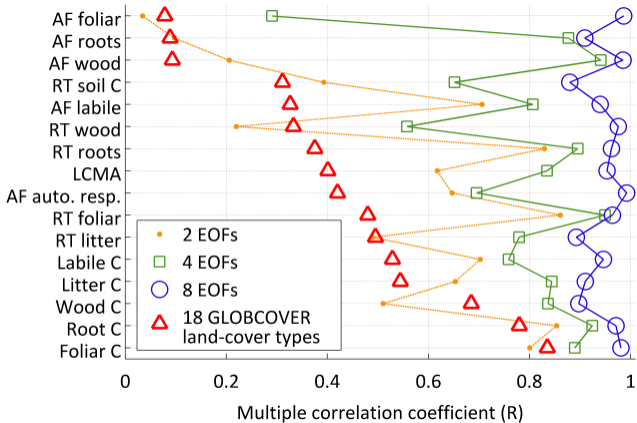












1 **Supporting information**

2  
3 **“The decadal state of the terrestrial carbon cycle: global retrievals of terrestrial carbon**  
4 **allocation, pools and residence times”.**

5  
6 **A. Anthony Bloom<sup>1,2,3</sup>, Jean-François Exbrayat<sup>2,3</sup>, Ivar van der Velde<sup>4</sup>, Liang Feng<sup>2,3</sup>, Mathew**  
7 **Williams<sup>2,3</sup>**

8  
9  
10 **1. Jet Propulsion Laboratory, California Institute of Technology, Pasadena, CA, USA**

11 **2. School of GeoSciences, University of Edinburgh, Edinburgh, UK**

12 **3. National Centre for Earth Observation, Edinburgh, UK**

13 **4. Wageningen University, Wageningen, The Netherlands**

14  
15  
16 **S1. Global 1° × 1° grid model-data fusion**

17  
18 **Global datasets.** We grid the 30-second Harmonized World Soil Database soil carbon (C) density  
19 (HWSD, based on national inventories of top 1 m soil bulk density and organic C content) (23)  
20 and a ~1km × 1km above- and below-ground pan-tropical biomass map (24) at 1° × 1°. We grid  
21 the MOD15A2 MODIS LAI product (1km × 1km) and a MODIS Burned Area product (0.25° ×  
22 0.25°) (34) at a 1° × 1° monthly resolution for each month within the period 2001-2010. While  
23 finer spatial/temporal resolutions can potentially be implemented, we chose a 1° × 1° monthly  
24 resolution as a consequence of the computational cost of our approach. We use ERA-interim 1°  
25 × 1° monthly re-analysis products as DALEC2 drivers; see (35) for MODIS quality flag and ERA-  
26 interim driver details. We exclude 1° × 1° grid-cells where desert and ice-covered areas account  
27 for more than 90% of the grid-cell land-cover (based on GLOBCOVER 2009 Global land-cover  
28 maps, 41), as their role in the terrestrial C cycle is negligible.

29  
30 **Model-data fusion.** Within each 1° × 1° degree grid cell  $i$ , we use the 1° × 1° aggregated biomass  
31 (tropics only), soil C and MODIS LAI datasets (observations  $\mathbf{O}_i$ ) to constrain DALEC2 parameters  $\mathbf{x}_i$   
32 (for a complete description of the DALEC2 model and C pools, we refer the reader to (35) and  
33 references therein). We implement a Metropolis-Hastings Markov Chain Monte Carlo  
34 (MHMCMC, 33, 35) to determine the probability of  $\mathbf{x}_i$  given observational constraints  $\mathbf{O}_i$  (see  
35 equation 1 in main text).

36  
37 The prior ranges of DALEC2 parameters  $\mathbf{x}_i$  are shown in Table S1. We also imposed a prior log-  
38 normal distribution on autotrophic respiration fraction  $x_{i,a}$  (autotrophic respiration =  $0.5 \times 1.2^{\pm 1}$ )  
39 and a prior log-normal distribution on canopy efficiency  $x_{i,c}$  (canopy efficiency parameter =  $17.5$   
40  $\times 1.2^{\pm 1}$ ), where  $\pm 1$  represents a normal distribution with mean 0 and variance 1. These  
41 constraints yield a range of results that are broadly consistent with the global GPP range  
42 reported by (30) and represent the range of autotrophic respiration estimates reported by (62).  
43 The prior parameter probability,  $\mathbf{p}(\mathbf{x}_i)$  is therefore expressed as:

44  
45

$$\mathbf{p}(\mathbf{x}_i) = \mathbf{p}_{\text{BW}}(\mathbf{x}_i) e^{-0.5 \left( \frac{\log(x_{i,a}) - \log(0.5)}{\log(1.2)} \right)^2} e^{-0.5 \left( \frac{\log(x_{i,c}) - \log(17.5)}{\log(1.2)} \right)^2}, \quad (1)$$

46 where  $\mathbf{p}_{\text{BW}}(\mathbf{x}_i)$  is the prior parameter probability described by (35). Within each  $1^\circ \times 1^\circ$  grid cell,  
 47 we prescribe an uncertainty factor of 1.5 to mean 2001-10 HWSO soil C and total above and  
 48 below-ground biomass density (i.e. mean labile + foliar + fine roots + wood), and an uncertainty  
 49 factor of 2 to mean monthly MODIS LAI observations. For total biomass, given that the  
 50 maximum entropy algorithm employed by (24) was based on bins of  $12.5 \text{ tC ha}^{-1}$ , we anticipate  
 51 that low biomass density values (such as the edges of the Sahel and Kalahari deserts) exhibit  
 52 comparable uncertainty. We therefore prescribe an uncertainty factor of  $\max(1.5, 12.5/B_i)$ ,  
 53 where  $B_i$  is the total biomass density and the  $\max()$  function denotes the maximum of the two  
 54 values. The likelihood function  $\mathbf{p}(\mathbf{O}_i|\mathbf{x}_i)$  is therefore expressed as:  
 55

$$\mathbf{p}(\mathbf{O}_i|\mathbf{x}_i) = \exp\left(-0.5 \sum_{j=1}^N \left(\frac{M_{ij} - O_{ij}}{U_{ij}}\right)^2\right), \quad (2)$$

56  
 57 where  $O_{ij}$  and  $U_{ij}$  are the  $j^{\text{th}}$  observations and uncertainty factors at location  $i$ , and  $M_{ij}$  is the  
 58 equivalent DALEC2 model output based on parameter vector  $\mathbf{x}_i$  (we note that  $O_{ij}$ ,  $U_{ij}$  and  $M_{ij}$  are  
 59 log-transformed, e.g. for a soil C value of  $100 \text{ tC ha}^{-1}$ ,  $O_{ij} = \log(100)$  and  $U_{ij} = \log(1.5)$ ). For each  
 60 LAI observation,  $M_{ij}$  is the DALEC2 foliar C (on the corresponding month) divided by leaf C mass  
 61 per leaf area. For biomass and soil C,  $M_{ij}$  is the DALEC2 soil C stock and mean live biomass (labile  
 62 + foliar + fine roots + wood) on Jan 1<sup>st</sup> 2001. For the analytical description of DALEC2, the  
 63 MHMCMC algorithm and  $\mathbf{p}_{\text{BW}}(\mathbf{x}_i)$ , we refer the reader to (35) and references therein; the DALEC2  
 64 fire module is described in section S3.  
 65

66 **Ecological and Dynamical Constraints.** The twelve Ecological and Dynamical Constraints (EDCs  
 67 1-12, 35) are a component of the prior parameter probability –  $\mathbf{p}_{\text{BW}}(\mathbf{x}_i)$  – and consist of relative  
 68 constraints on allocation parameters, turnover rates, growth rates, exponential decays and  
 69 steady state proximity. When steady state is not assumed, steady state proximity conditions are  
 70 necessary to distinguish between real and nonsensical C pool trajectories (35). We developed a  
 71 simpler numeric equivalent of the steady state proximity EDCs (EDCs 9-12), to account for the  
 72 stochastic C losses from fires. For each pool, we derive the steady state proximity factor ( $S_{\text{prox}}$ )  
 73 as follows:  
 74

$$S_{\text{prox}} = \frac{\overline{C_{\text{input}}}}{\overline{C_{\text{output}}}}, \quad (3)$$

75  
 76  
 77  
 78 where  $\overline{C_{\text{input}}}$  and  $\overline{C_{\text{output}}}$  are the mean inputs and outputs from each pool. We impose a  
 79 steady state proximity condition of  $0.5 > S_{\text{prox}} > 2$  for each pool.  
 80

81 We found that EDC 8 – the ecological and dynamic constraint limiting rapid exponential pool  
 82 trajectories – was excessively rigid for relatively small amounts of exponential pool trajectories  
 83 (which can occur naturally and/or as a model artifact). Here we use a simpler approach to  
 84 minimize the rapid exponential decay of C pools: we ensure that the steady state proximity of  
 85 each C pool at time zero –  $S_{\text{prox}(\text{jan2001})}$  – is within 0.05 of  $S_{\text{prox}}$ , i.e.  
 86

$$|S_{\text{prox}} - S_{\text{prox}(\text{jan2001})}| < 0.05. \quad (4)$$

87  
 88  $S_{\text{prox}(\text{jan2001})}$  can be derived as:

89

$$S_{prox(jan2001)} = S_{prox} \times \frac{\overline{C_{jan2001-10}}}{C_{jan2001}}, \quad (5)$$

91

92 where  $\overline{C_{jan2001-10}}$  is the mean January C pool stock and  $C_{(Jan2001)}$  is the C pool stock in January  
 93 2001. The CARDAMOM code used in this manuscript (DALEC2 model, EDCs and adaptive  
 94 Metropolis-Hastings Markov Chain Monte Carlo) is available upon request.

95

## 96 S2. DALEC2 fire module

97

98 To determine the monthly C losses from fires at time  $t$ , we determine the monthly fraction of  
 99 each grid cell burned,  $B_{area(t)}$ , based on the MODIS-derived burned area product (34). At each  
 100 monthly time step, the fire losses within each  $1^\circ \times 1^\circ$  grid cell are derived as follows:  
 101

$$F_{e(t)} = B_{area(t)} \times \sum_{p=1}^6 k_{factor(p)} C_{(p,t)}, \quad (6)$$

102 where  $F_{e(t)}$  are the total fire C emissions at time  $t$ ,  $k_{factor(p)}$  is the combustion factor for pool  $p$ , and  
 103  $C_{(p,t)}$  is the C in pool  $p$  at time  $t$ . We also impose a resilience factor  $r$  to the remaining pools  
 104 within the burned area: from live biomass pool, a fire-mortality flux is derived from the un-  
 105 combusted C pools as follows:  
 106

$$F_{m(t,p)} = B_{area(t)} \times (1 - k_{factor(p)}) (1 - r) C_{(p,t)}, \quad (7)$$

107

108 The fire-mortality C flux from foliage, roots and labile is deposited into the litter pool, and fire  
 109 mortality C flux from wood is transferred to the soil C pool. Equally,  $(1 - r)$  of un-combusted litter  
 110 C is transferred to the soil C pool. The  $k_{factor}$  values for labile (0.1), foliar (0.9), root (0.1), wood  
 111 (0.1), litter (0.5) and soil C (0.01) are broadly equivalent to the  $k_{factor}$  values used by the Global  
 112 Fire Emission Database (37). We apply a resilience factor of  $r = 0.5$ . The sensitivity calculations  
 113 associated with  $k_{factor(p)}$  and  $r_f$  are described in section S4.

114

## 115 S3. Global state and process variables

116

117 The spatial distributions of individual C pool allocation fractions, residence times and stocks are  
 118 shown in Fig. S1. The residence time for each C pool at grid cell  $i$  is derived as follows:  
 119

$$RT_{pool(j)} = \frac{C_{pool(j)}}{F_{in(j)} - \Delta C_{pool(j)}} \times 365.25, \quad (8)$$

120

121 where  $C_{pool(j)}$  is the mean pool size,  $F_{in(j)}$  is the mean daily C pool input and  $\Delta C_{pool(j)}$  is the  
 122 mean daily change in pool size throughout 2001-10 for the  $j^{th}$  parameter vector sample of  $\mathbf{y}_i$  (i.e.  
 123  $C_{pool(j)}$ ,  $F_{in(j)}$  and  $\Delta C_{pool(j)}$  are calculated from DALEC2 output driven with  $j^{th}$  parameter  
 124 vector sample of  $\mathbf{y}_i$ ). Mean live biomass (dead organic matter) pool residence times are derived  
 125 based on equation 8, where  $C_{pool(j)}$ ,  $F_{in(j)}$  and  $\Delta C_{pool(j)}$  are the total live biomass (dead  
 126 organic matter) C corresponding to  $j^{th}$  parameter vector sample of  $\mathbf{y}_i$ . Leaf lifespan is equivalent  
 127 to  $RT_{foliar}$ . Reported global and zonal 25<sup>th</sup> – 75<sup>th</sup> %ile ranges of total annual fluxes were derived  
 128 from the sum of monthly  $1^\circ \times 1^\circ$  25<sup>th</sup> and 75<sup>th</sup> %iles for each flux multiplied by the  $1^\circ \times 1^\circ$  grid  
 129 cell area; the same approach was used to derive median fluxes and mode net C exchange (NCE).

130 Monthly mode NCE within each  $1^\circ \times 1^\circ$  grid-cell was derived by binning NCE samples into 0.01  
131  $\text{gC m}^{-2} \text{ day}^{-1}$  intervals.

132

#### 133 **S4. Sensitivity Tests**

134

135 We determine the sensitivity of C allocation, residence times and C pool size estimates at  
136 locations B, T, D and W (see Materials and Methods in main text for B, T, D and W coordinates)  
137 to LAI, biomass and soil C data constraints (sensitivity tests S1-S6), fire combustion and  
138 resilience factor coefficients (sensitivity test S7-S10), the use of MPI GPP (36) instead of the  
139 default DALEC (19) GPP (sensitivity test S11), and the suppression of heterotrophic respiration  
140 under  $-10^\circ\text{C}$  (sensitivity test S12). The sensitivity experiments are summarized in Table S2. The  
141 results of the sensitivity tests are shown in Fig. S2.

142

#### 143 **S5 Comparison against in-situ and regional observations**

144

145 CARDAMOM results are compared against a range of in-situ measurements in Table S3. We  
146 compare each in-situ measurement against the 50% and 90% confidence range of the mean  $1^\circ \times$   
147  $1^\circ$  values within the stated region. Comparison details and footnotes are included in Table S3.  
148 We also compare CARDAMOM total biomass against a boreal forest biomass dataset derived  
149 from synthetic aperture radar data (BIOMASAR map, 40) aggregated to  $1^\circ \times 1^\circ$ . The  
150 CARDAMOM-to-BIOMASAR comparison is conducted for the total biomass across all  $1^\circ \times 1^\circ$   
151 areas with at least 95% BIOMASAR map coverage; total BIOMASAR biomass within those areas is  
152 38% lower than CARDAMOM biomass. We note that lower-than-expected LCMA estimates in  
153 boreal ecosystems (Fig. 6) could be explained by (i) understory plant traits (linked to deciduous  
154 shrubs); or (ii) seasonal MODIS LAI biases (53). In particular, the significant correlation between  
155 LCMA and leaf lifespan suggests that retrieved LCMA accuracy could be strongly linked to  
156 seasonal biases in MODIS LAI.

157

#### 158 **S6 Comparison to GLOBCOVER land-cover types and EOFs**

159

160 For each  $1^\circ \times 1^\circ$  grid cell  $i$  we determine the fraction of each GLOBCOVER (41) land-cover type  $L$ ,  
161  $F_{L(i)}$ . We then determine the Pearson's correlation coefficients ( $r_{LS}$ ) between  $\mathbf{f}_L$  (the vector of all  
162  $1^\circ \times 1^\circ$  land-cover type  $L$  fractions) and each C state and process variable vector  $\mathbf{c}_S$  (the vector of  
163 each  $1^\circ \times 1^\circ$  state and process variable): state or process variables (denoted by subscript  $S$ )  
164 consist of allocation fractions, C residence times, C pool sizes and leaf C mass per leaf area. The  
165  $r_{LS}^2$  values between each GLOBCOVER land-cover type fraction  $L$  and each C state/process  
166 variable  $S$  are shown in Fig. S3. The land-cover categories are: irrigated croplands (**CRI**); Rainfed  
167 croplands (**CRR**); Mosaic cropland > vegetation (**MCV**); Mosaic vegetation > cropland (**MVC**);  
168 Closed to open broadleaved evergreen or semi-deciduous forest (**BESDF**); Closed broadleaved  
169 deciduous forest (**BDF**); Open broadleaved deciduous forest/woodland (**BDFW**); Closed (>40%)  
170 needleleaved evergreen forest (**NEF**); Open needleleaved deciduous or evergreen forest (**NDEF**);  
171 Closed to open mixed forest (**MF**); Mosaic forest or shrubland > grassland (**MFSG**); Mosaic  
172 grassland > forest or shrubland (**MGFS**); Closed to open shrubland (**SRB**); Closed to open  
173 herbaceous vegetation (**GRA**); Sparse vegetation (**SPA**); Closed to open broadleaved forest  
174 regularly flooded (**FWE**); forest or shrubland, permanently flooded (**SWE**); Closed to open  
175 vegetation on flooded or waterlogged soil (**WET**) (54).

176

177 The multiple correlation coefficient  $R_S$  between C state/process variable  $S$  and 18 GLOBCOVER  
178 land-cover type fractions is derived as follows:  
179

$$R_S = \mathbf{r}_S^T \mathbf{R}_{LL}^{-1} \mathbf{r}_S, \quad (9)$$

180  
181 where  $\mathbf{r}_S$  is the  $1 \times 18$  vector of correlations coefficients between state/process variable vector  $\mathbf{c}_S$   
182 and 18  $1^\circ \times 1^\circ$  land-cover type fraction vectors  $\mathbf{f}_L$ ,  $\mathbf{r}_S^T$  is the transpose of  $\mathbf{r}_S$ , and  $\mathbf{R}_{LL}^{-1}$  is the inverse  
183 of the correlation matrix  $\mathbf{R}_{LL}$ , which contains the inter-correlations between 18 land-cover type  
184 fraction vectors  $\mathbf{f}_L$ .  $R_S$  is equivalent to the maximum correlation (Pearson's  $r^2$ ) between the  
185 spatial variability of C state/process variable  $\mathbf{c}_S$  and the best-fitting linear combination of land-  
186 cover type fractions  $\mathbf{f}_L$ . The resulting  $R_S$  values are shown in Fig. 6 (main text).  
187  
188

189 We also employ a multiple correlation coefficient analysis on the empirical orthogonal functions  
190 (EOFs, or the "primary modes" of variability) of all  $\mathbf{c}_S$ . We conducted a principal component  
191 analysis to derive the eight primary EOFs (EOFs were derived using "pca.m" function in Matlab;  
192 each  $\mathbf{c}_S$  vector is centered at zero and scaled to the standard deviation of  $\mathbf{c}_S$ ). Standardized EOFs  
193 (normalized by EOF standard deviation) and EOF coefficients are shown in Fig. S4. The EOF maps  
194 exhibit the primary modes of  $\mathbf{c}_S$  variability in space; for each  $\mathbf{c}_S$ , the maximum spatial variability  
195 explained by EOFs 1 – N is the sum of standardized EOFs 1 – N multiplied by their associated  
196 coefficients. EOF multiple correlation coefficients –  $R_{S(EOF)}$  – were derived for the primary two,  
197 four and eight EOFs based on equation 9, where  $\mathbf{R}_{LL}$  is the identity matrix (as EOFs are  
198 orthogonal).  $R_{S(EOF)}$  results are shown in Fig. 6 in the main text.  
199

### 200 ***S7 Comparison against the MstMIP terrestrial biosphere model ensemble***

201  
202 We compare GPP, ecosystem respiration and NCE against the MstMIP terrestrial biosphere  
203 model ensemble Version 1.0 (64) net C exchange (note: total C exchange reported as net  
204 ecosystem exchange, or 'NEE', by MstMIP). The  $0.5^\circ \times 0.5^\circ$  monthly GPP, total (heterotrophic  
205 and autotrophic) respiration and NCE values for 2001-10 – based on the BG1 simulation – were  
206 downloaded from (<http://nacp.ornl.gov/mstmipdata/>), and were aggregated to a  $1^\circ \times 1^\circ$  grid  
207 (the BG1 simulation includes time-varying nitrogen deposition, atmospheric  $\text{CO}_2$  and land-use  
208 history (22)). The eight MstMIP models shown in Fig. S5 are BIOME-BGC, CLASS-CTEM-N,  
209 CLM4VIC, CLM4, DLEM, ISAM, TEM6, TRIPLEX-GHG (for the sake of brevity, we did not label each  
210 individual MstMIP model in Fig. S5);  
211

### 212 ***S8 Atmospheric $\text{CO}_2$ comparison***

213  
214 We incorporated the 2009-2010 CARDAMOM monthly mode net C exchange (NCE) values into  
215 the GEOS-Chem atmospheric chemistry and transport model (29). The GEOS-Chem model  
216 simulations are based on GEOS-Chem version 8.2, driven by NASA GEOS-5 meteorological fields.  
217 In addition to NCE, fossil fuel emissions and oceanic surface  $\text{CO}_2$  fluxes are prescribed (56). We  
218 compared the 2009-2010 GEOS-Chem model  $\text{CO}_2$  concentrations against the monthly mean  
219 anomaly across 12 Total Carbon Column Observing Network sites (TCCON, 38): Bialystok,  
220 Poland; Darwin, Australia; Eureka, Canada; Garmisch, Germany; Karlsruhe, Germany; Lauder,  
221 New Zealand; Lauder, New Zealand; Lamont, Oklahoma; Orleans, France; Park Falls, Wisconsin;  
222 Sodankyla, Finland; Wollongong, Australia. Details of the GEOS-Chem TCCON comparison are  
223 reported by (63) and references therein. We note that the uncertainty in the GEOS-Chem trend

224 due to CARDAMOM flux uncertainty is substantial: global NCE 25<sup>th</sup> – 75<sup>th</sup> percentile = -8 – +13Pg  
225 C yr<sup>-1</sup>, which roughly corresponds to a ±5ppm growth rate (1). To evaluate the CARDAMOM  
226 seasonal NCE variability, we compare the linearly de-trended model and observations (Fig. S6).

227  
228

## 229 Figures

230

231 **Fig. S1: Left two columns:** posterior GPP C allocation to autotrophic respiration (equivalent to 1  
232 – C use efficiency), labile C, foliar C, fine roots, wood (mean, left column) and associated  
233 uncertainty (standard deviation, right column). **Middle two columns:** Posterior C residence time  
234 in foliar C, fine roots, wood, litter and soil C (log-based mean, left column) and associated  
235 uncertainty factors (based on logarithmic standard deviation, right column). **Right two columns:**  
236 Posterior mean 2001-10 C stocks in labile, foliar, fine roots, wood, litter C pools (mean, left  
237 column) and associated uncertainties (standard deviation, right column).

238

239 **Fig. S2.** Posterior median and 50% confidence ranges shown for 1° × 1° grid-cells B, T, D and W  
240 shown for the unperturbed results (S0) and sensitivity experiments S1-S12. The coordinates of B,  
241 T, D and W are reported in the Materials and Methods (locations shown in inset map). Across all  
242 locations, 88% of median sensitivity analysis estimates (sensitivity tests S1-S12) are within ±50%  
243 of unperturbed median C state and process variable retrievals.

244

245 **Fig. S3.** Pearson correlation coefficients ( $r^2$ , shown in color bar) between GLOBCOVER land-cover  
246 types fractions (x-axis) and C state and process variables (y-axis), based on their correlation  
247 across all 1° × 1° grid cells within the global study area. See section S5 for land-cover type  
248 acronyms.

249

250 **Fig. S4: Maps:** Eight primary 1° × 1° standardized empirical orthogonal functions (EOFs 1-8)  
251 derived from a principal component analysis of standardized C state and process variables (see  
252 section S6). The two dominant modes (EOF1 and EOF2) together reflect first-order global  
253 variations in C state/process variables ( $c_s$ ) due to in latitude and precipitation, while higher order  
254 modes reflect increasingly complex spatial structures (however, EOFs 3-8 typically account for a  
255 smaller portion of  $c_s$  spatial variability). **Scatter plots:** standardized EOF 1-8 coefficients  
256 corresponding to each C state/process variable (shown as symbol-color combinations). The  
257 linear sum of standardized EOFs 1-4 (1-8) and their associated coefficients reproduces 29-95%  
258 (88-99%) of C state/process variability (see Fig. 6 in the main text).

259

260 **Fig. S5:** CARDAMOM zonal profiles of median gross primary production, ecosystem respiration,  
261 fires and net C exchange (red). The 50% confidence range is depicted as a light-pink shaded  
262 area. The blue lines represent the 8 global MsTMIP models (64; see section S7 for details). The  
263 dashed black line denotes the flux-tower derived GPP (36). The continuous black line denotes  
264 the GFED version 3 total C emissions (36).

265

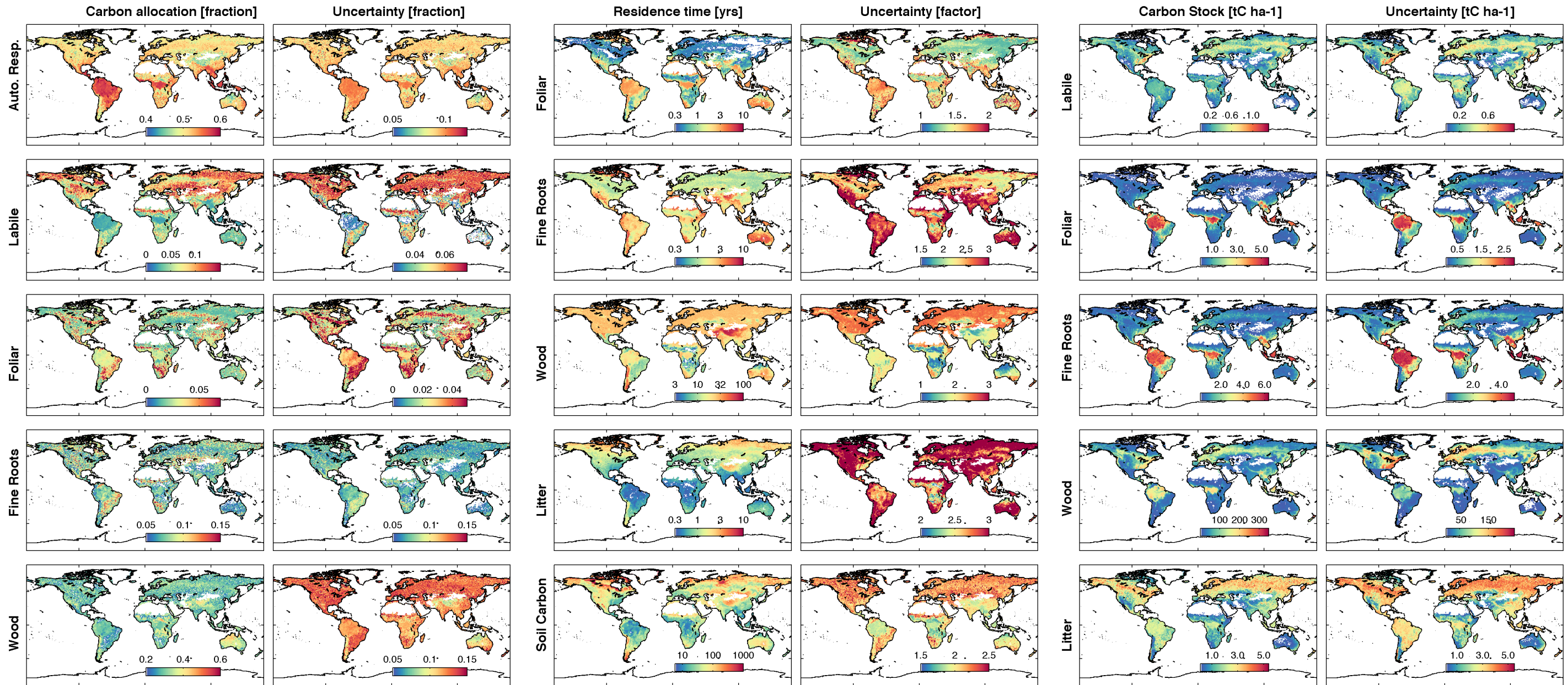
266 **Fig. S6.** 2009-2010 GEOS-Chem model - with CARDAMOM mode NCE - compared against mean  
267 monthly TCCON atmospheric column measurements across 12 TCCON sites: the left panel shows  
268 atmospheric CO<sub>2</sub> concentrations, and the right panel shows the linearly de-trended CO<sub>2</sub>  
269 anomalies. The de-trended comparison Pearson's  $r = 0.93$  and RMSE = 0.53 ppm.

270

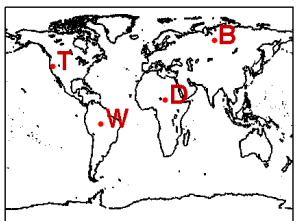
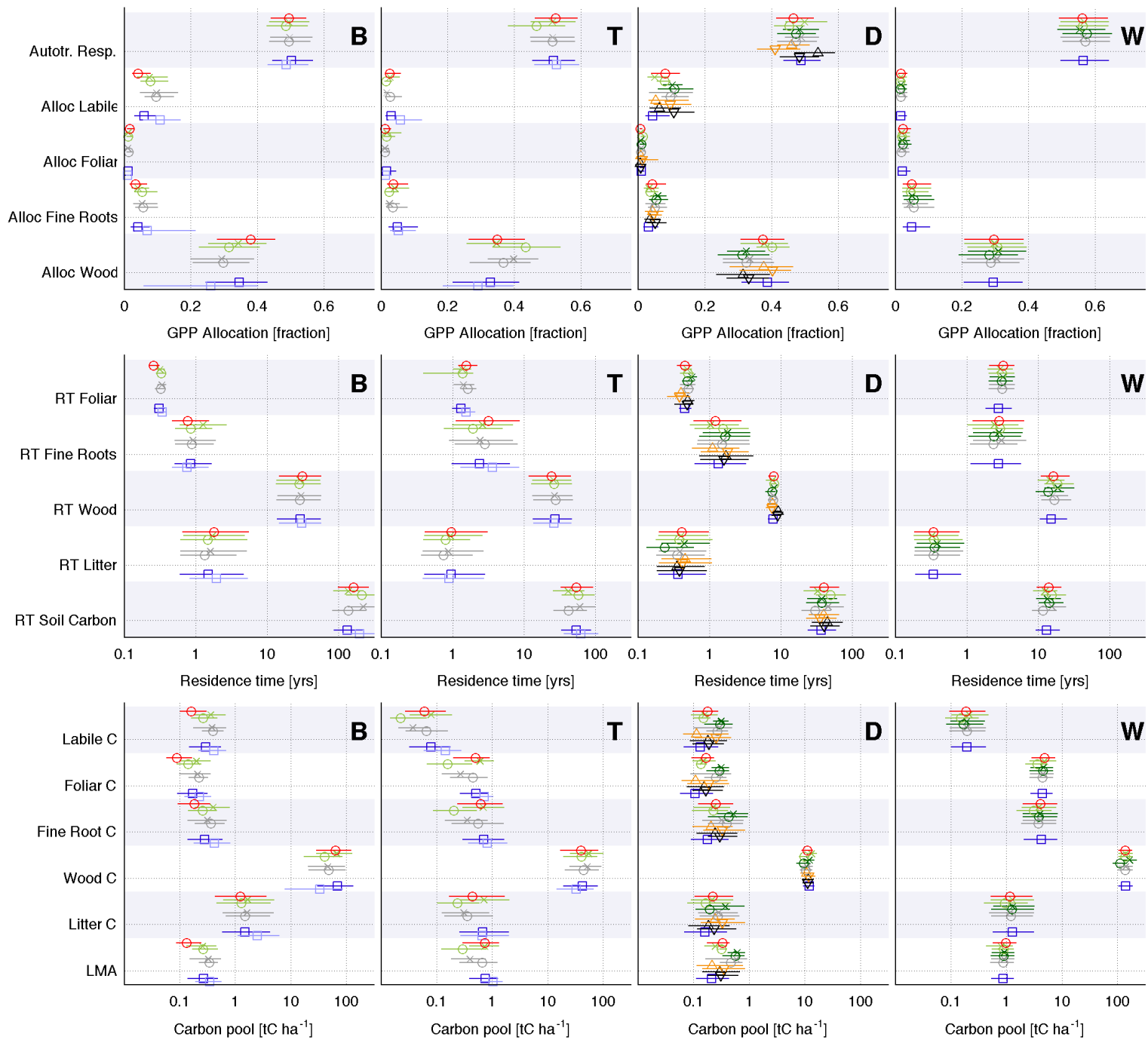
271

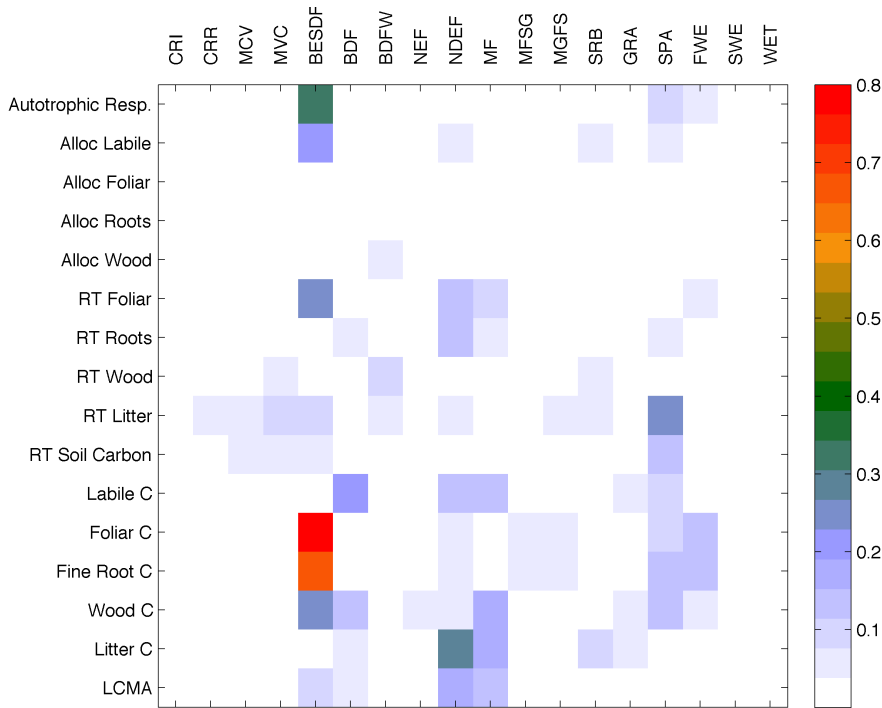


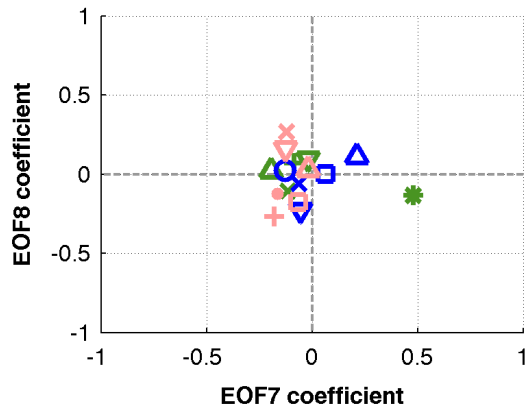
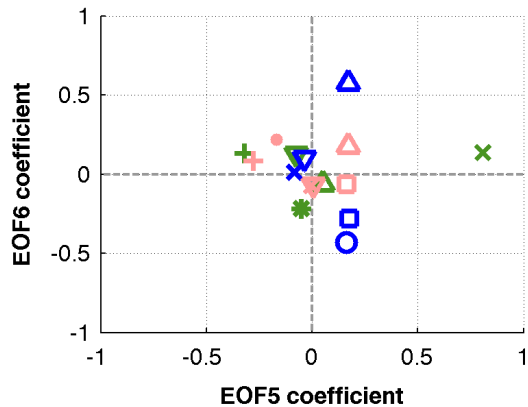
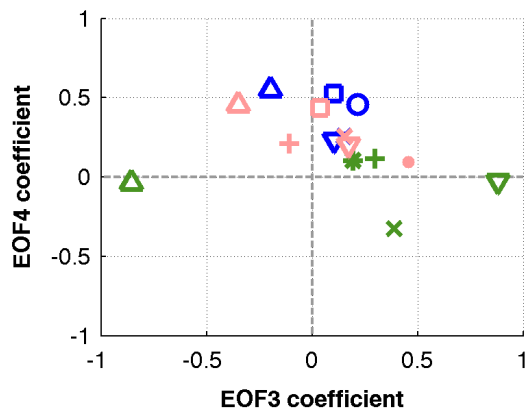
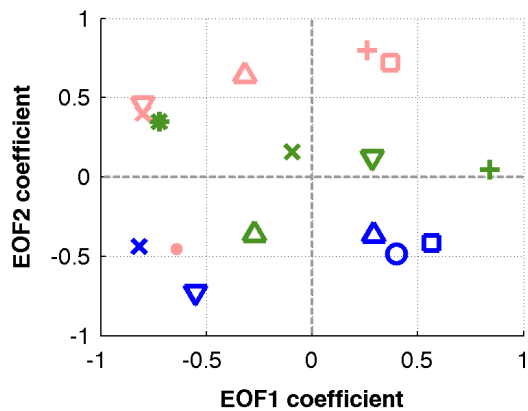
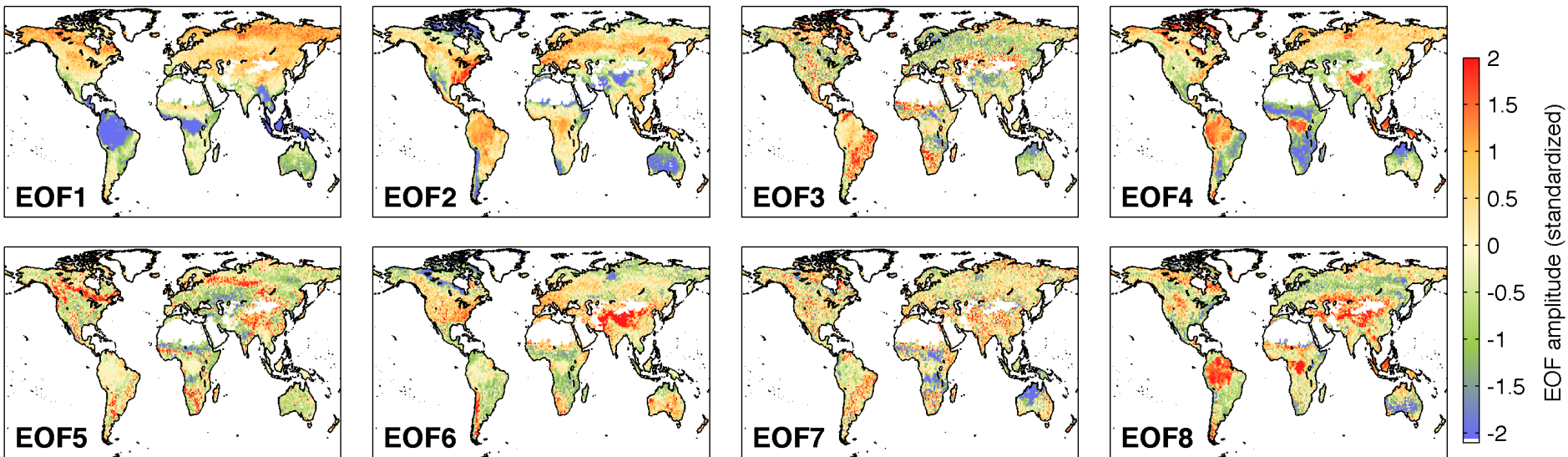
272	<b>Tables</b>
273	
274	<b>Table S1:</b> DALEC2 parameters, descriptions and prior ranges (the DALEC2 equations are fully
275	described in (35)).
276	
277	<b>Table S2:</b> Sensitivity tests for C allocation, residence times and C pool size estimates at locations
278	B, T, D and W.
279	
280	<b>Table S3:</b> In-situ observations and CARDAMOM posterior state and process variable estimates.
281	



- Unperturbed
- × S1. +20% MODIS LAI
- S2. -20% MODIS LAI
- × S3. +20% Tropical Biomass
- S4. -20% Tropical Biomass
- × S5. +20% HWSO soil carbon
- S6. -20% HWSO soil carbon
- △ S7. +20% combustion factor
- ▽ S8. -20% combustion factor
- △ S9. +20% fire resilience
- ▽ S10. -20% fire resilience
- S11. MPI GPP
- S12. No heterotrophic resp. at <-10°C





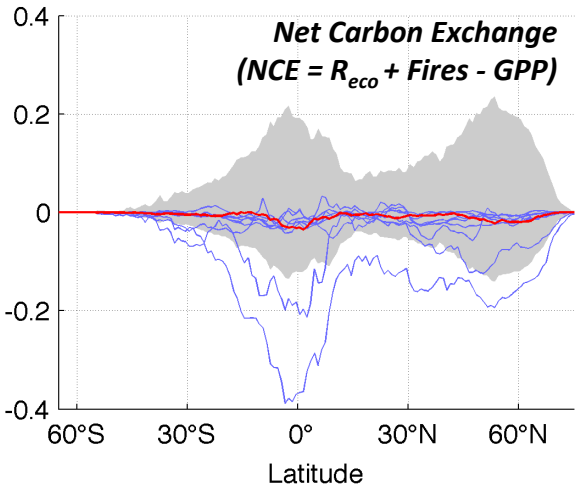
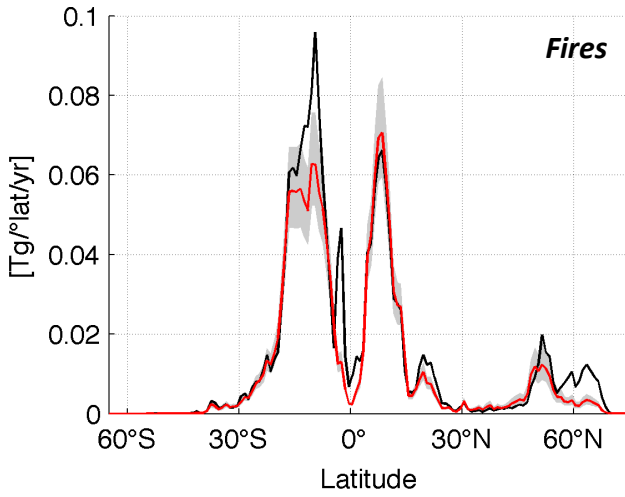
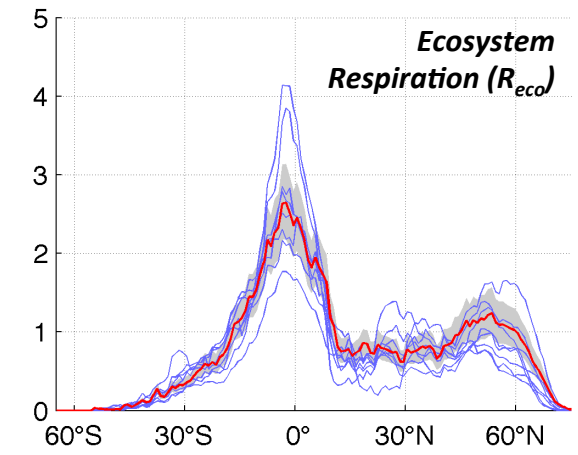
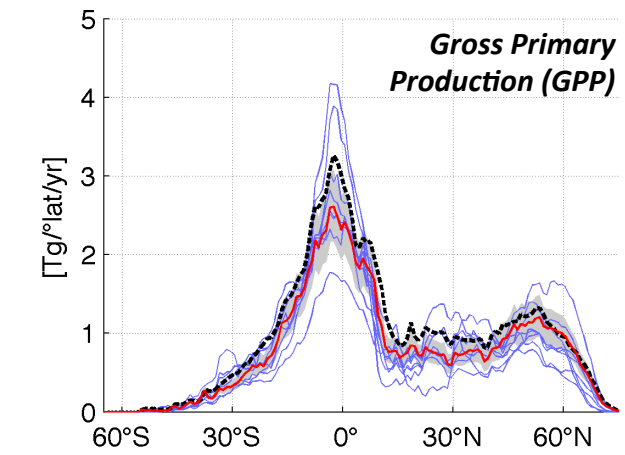


**Symbols**

- \* Auto. resp.
- + Labile
- × Foliar
- ▽ Fine root
- △ Wood
- Litter
- Soil carbon
- LCMA

**Colors**

- Allocation (Green)
- Residence time (Blue)
- Carbon stocks (Red)



**CARDAMOM**  
*median (mode for NCE)*

**CARDAMOM**  
*50% C.R.*

**FLUXNET**  
**derived GPP**  
*Jung et al., 2009*

**MsTMIP models**  
*Huntzinger et al., 2013.*

**GFEDv3**  
*van der Werf et al., 2010*

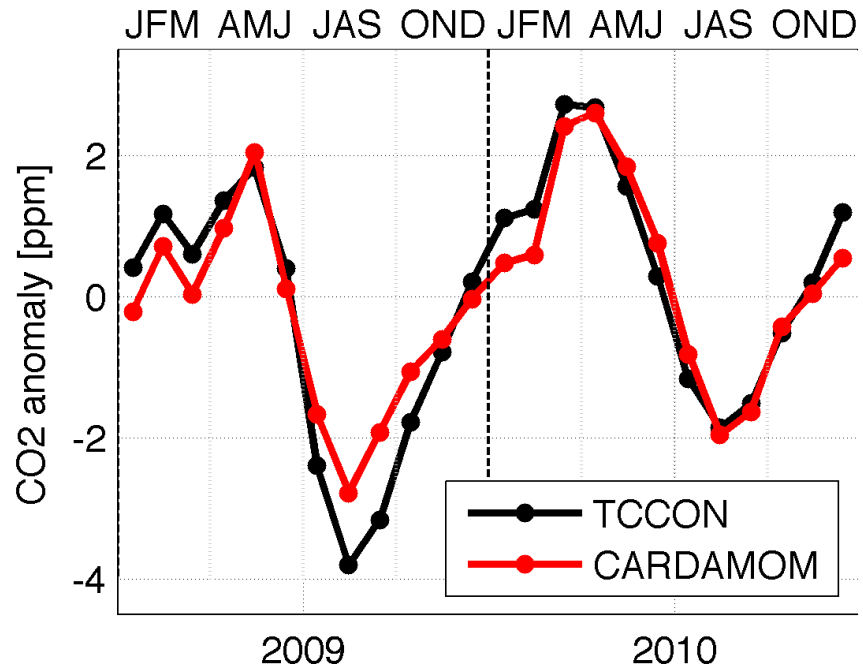
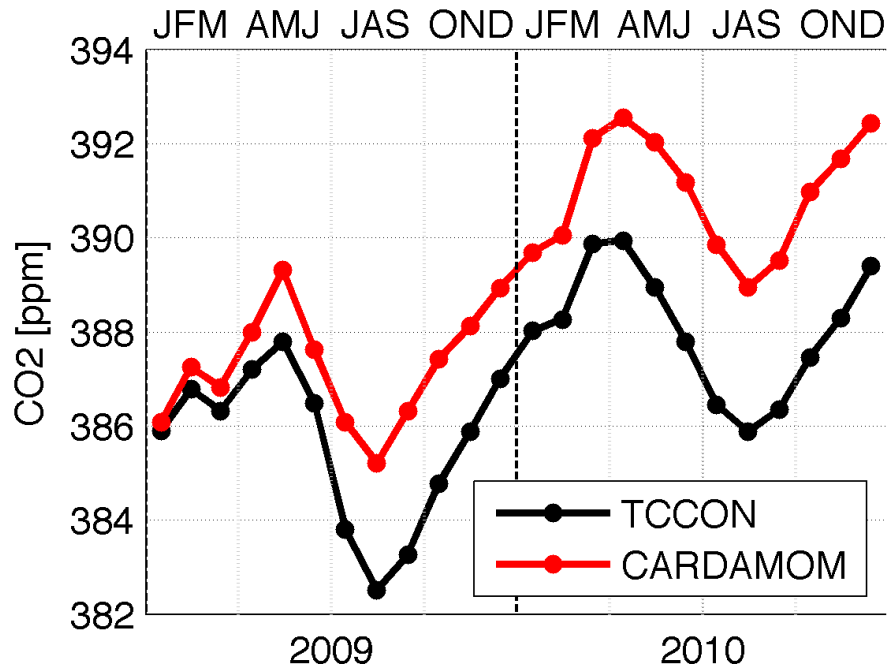


**Table S1:** DALEC2 parameters, descriptions and prior ranges (the DALEC2 equations are fully described in (35)).

	<b>Parameters</b>	<b>Prior Range</b>
Allocation fractions	Autotrophic Respiration	0.2-0.8*
	Labile	0.01-0.5
	Foliage	0.01-0.5
	Fine roots	0.01-0.5
	Wood	0.01-0.5
Turnover rates	Woody C turnover rate	$2.5 \times 10^{-5} - 10^{-3} \text{ d}^{-1}$
	Fine root turnover rate	
	Litter turnover rate	$10^{-4} - 10^{-2} \text{ d}^{-1}$
	Soil organic C turnover rate	$10^{-4} - 10^{-2} \text{ d}^{-1}$
	Litter mineralization rate	$10^{-7} - 10^{-3} \text{ d}^{-1}$
	Exponential temperature dependence	$10^{-2} - 10^{-5} \text{ d}^{-1}$
		0.018–0.08
Canopy parameters	Leaf onset day	1-365.25
	Leaf fall day	1-365.25
	Canopy efficiency	5 – 50*
	Leaf C mass per leaf area (LCMA)	5 - 200 gC m <sup>-2</sup>
	Annual leaf loss fraction	1/8 – 1
	Labile C release period	10 – 100 days
	Leaf fall period	20 – 150 days
Initial C stocks	Labile C	1-2000gC m <sup>-2</sup>
	Foliar C	1-2000gC m <sup>-2</sup>
	Fine root C	1-2000gC m <sup>-2</sup>
	Litter C	1-2000gC m <sup>-2</sup>
	Above & Below ground wood	1 - 100,000gC m <sup>-2</sup>
	Soil C (1m depth)	1 - 200,000gC m <sup>-2</sup>

\* Autotrophic Respiration and Canopy efficiency parameter log-normal prior distributions are described in section S1.



**Table S2:** Sensitivity tests for C allocation, residence times and C pool size estimates at locations B, T, D and W.

<b>Sensitivity Test(s)</b>	<b>Description</b>
S1 & S2	+20% & -20% in LAI observations
S3 & S4	+20% & -20% increase in biomass observations
S5 & S6	+20% & -20% increase in HWSO Soil Carbon observations
S7 & S8	+20% <sup>1</sup> & -20% increase in fire combustion factors
S9 & S10	+20% & -20% increase in fire resilience factor
S11	Use mean 1° × 1° aggregated MPI GPP (36) as driver
S12	No heterotrophic respiration <sup>2</sup> under -10°C

<sup>1</sup>Foliar combustion factor increase by 10% (from 0.9 to 0.99).

<sup>2</sup>Respiration temperature dependence coefficient (19) set to zero at <-10°C, scaled by unity at >0°C, and scaled from 0 to 1 between -10°C and 0°C.

**Table S3:** In-situ observations and CARDAMOM posterior state and process variable estimates.

Measurement (region)	CARDAMOM range*	In-situ observations (study)
Fine roots (Amazon river basin)	9.2 – 10.8 tC ha <sup>-1</sup> (2.8 – 11.5 tC ha <sup>-1</sup> )	5 – 8 tC ** ha <sup>-1(a)</sup> (65)
Fine roots (North-East U.S.; >30°N, >100°W)	1.6 – 3.3 tC ha <sup>-1</sup> (0.9 – 6.0 tC ha <sup>-1</sup> )	1.25 tC ** ha <sup>-1(a)</sup> (66)
Fine root residence time (North-East U.S., >30°N, >100°W)	1.1 – 1.5 yrs (0.9 – 3.2 yrs)	0.83 – 1.25 yrs <sup>(a)</sup> (66)
Fine root RT (global: where woody C > 10tC ha <sup>-1</sup> )	1.2 – 2.6 yrs (0.9 – 4.7 yrs)	1.25 – 2.5 yrs <sup>(b)</sup> (67)
Wood Carbon RT (Amazon river basin)	15 – 21 yrs (9 – 24 yrs)	~20 – 70yrs <sup>(b)</sup> (20, above-ground only)
Carbon Use Efficiency (CUE) *** (Amazon river basin)	0.42 – 0.43 (0.42 – 0.45 )	Amazon field sites: 0.32 – 0.47 <sup>(b)</sup> (39)
Fine root C (Lat > 66°N)	0.3 – 0.4 tC ha <sup>-1</sup> (0.2 – 0.6 tC ha <sup>-1</sup> )	Arctic Ecosystems: 0.1 – 5 tC ha <sup>-1(b)</sup> (68)

\* Area-weighted 25<sup>th</sup> – 75<sup>th</sup> %ile (5<sup>th</sup> – 95<sup>th</sup> %ile) 1° × 1° C state and process variables (see Materials and Methods).

\*\* Dry mass to C mass conversion factor = 0.5

\*\*\* CUE = 1 – autotrophic respiration fraction

<sup>a</sup>Individual site range

<sup>b</sup>regional or global range